Atmospheric Aerosol over Vermont: Chemical Composition and Sources

Alexander V. Polissar and Philip K. Hopke

Department of Chemical Engineering, Clarkson University, Potsdam, New York 13699-5810

Richard L. Poirot

VT Air Pollution Control Division, 103 South Main Street, Building 3 South, Waterbury, Vermont 05671-0402

ENVIRONMENTAL SCIENCE & TECHNOLOGY

Reprinted from
Volume 35, Number 23, Pages 4604–4621

Environ. Sci. Technol. 2001, 35, 4604–4621

Atmospheric Aerosol over Vermont: Chemical Composition and Sources

ALEXANDER V. POLISSAR AND PHILIP K. HOPKE*

Department of Chemical Engineering, Clarkson University, Potsdam, New York 13699-5810

RICHARD L. POIROT

VT Air Pollution Control Division, 103 South Main Street, Building 3 South, Waterbury, Vermont 05671-0402

Aerosol chemical composition data for $PM_{2.5}$ samples collected during the period from 1988 to 1995 at Underhill, VT, were analyzed. Sulfur and black carbon mass concentrations ranged from 0.01 to 6.5 $\mu g\ m^{-3}$ and from 0.05 to 2.2 $\mu g\ m^{-3}$, respectively, while the total fine aerosol mass concentration ranged from 0.2 to 51.1 $\mu g\ m^{-3}$. Seasonal variations with maxima during the summer and minima in winter/spring were observed for sulfur and the fine mass concentrations. No annual pattern was observed for black carbon. Seasonal variations for most of the other anthropogenic species had maxima in winter and spring and minima in the summer. A factor analysis method, positive matrix factorization (PMF), utilizing error estimates of the data to provide optimum data point scaling was used to obtain information about possible sources of the aerosol. An 11-factor solution was obtained. The six sources representing wood burning, coal and oil combustion, coal combustion emissions plus photochemical sulfate production, metal production plus municipal waste incineration, and emissions from motor vehicles were identified. Emissions from smelting of nonferrous metal ores, arsenic smelting, and soil particles and particles with high concentrations of Na were also identified by PMF. Potential source contribution function (PSCF) analysis combines the aerosol data with the air parcel backward trajectories. PSCF was applied to identify possible source areas and pathways that give rise to the observed high particulate mass concentrations from these 11 sources. The CAPITA Monte Carlo trajectory model was used to obtain 10 sets of 5-day air parcel back trajectories arriving every 2 h for the 7-yr period from 1988 to 1995. The PSCF plot for the black carbon factor shows high probabilities in the area surrounding the sampling site, indicating a strong local influence from residential wood combustion in northern New England and southwestern Quebec. Similar large potential source areas in the midwestern United States were identified for the two coal combustion factors. The midwestern United States was also identified as the source region for the Zn–Pb factor. The oil combustion factor was associated with the east coast of the United States. The results for the Pb–Mn factor suggests high probability over the nearby Montreal urban area and the areas in the midwestern United States. The windblown dust emissions from the areas to the north are significant contributors for the soil factor. Canadian Ni smelters are the main sources for the As factor, although there is some contribution from coal-fired power plants to the south and west of Underhill, VT. It is concluded that the combination of the two receptor modeling methods, PMF and PSCF, provides an effective way in identifying atmospheric aerosol sources and their likely locations. Emissions from different anthropogenic activities as well as secondary aerosol production are the main sources of aerosol measured in Vermont. Fuel combustion, local wood smoke, municipal waste incineration, and the secondary sulfate production collectively accounted for about 87% of the fine mass concentrations measured in Vermont.

Introduction

Fine particles in the atmosphere are related to emissions from a wide range of natural and anthropogenic sources. The presence of anthropogenic aerosol in the atmosphere may result in changes in the solar radiation balance and visibility (*1*). For this reason, the investigation of the spatial and temporal variations of the aerosol concentration and the identification of possible sources of aerosol are important. The results of the investigation could be useful for the understanding of mechanisms of transport and transformation of the atmospheric aerosol. Receptor models, which attribute pollution to sources through statistical and/or meteorological interpretation of data, represent a useful approach to the investigation of the aerosol (*2*). This paper reports the results of the study of seasonal variability and sources of fine particles over Vermont for the period from 1988 to 1995. A new factor analysis method, positive matrix factorization (PMF) (*3*), utilizing error estimates of the data to provide optimum data point scaling was used to obtain information about possible sources of the aerosol sampling at Underhill, VT. A back trajectory-based method, potential source contribution function (PSCF), was used to help identify the likely locations of the identified sources. These methods are then compared with two other receptor models in ref *4*. In this paper, the data are first summarized graphically to identify potential source influences before presenting the more quantitative PMF and PSCF results.

Sampling and Analysis

Aerosol sampling in Underhill, VT (44.53 N, 72.86 W, 400 m elevation), was conducted between September 1988 and June 1995 as a part of the *I*nteragency *M*onitoring of *PRO*tected *V*isual *E*nvironments (IMPROVE) network, a consortium of EPA and Federal land management agencies (*5*, *6*), and the NESCAUM Regional Particle Monitoring Network (*7*). The IMPROVE/NESCAUM sampler was programmed to automatically collect two 24-h duration samples per week on Wednesdays and Saturdays and also every sixth day (routine EPA PM_{10} sampling schedule), with a resultant data set of 853 samples with 28 measured variables. The IMPROVE sampler consists of a size-selective inlet, a cyclone to provide a particle size cutoff based on the flow rate, the collection substrates, a critical orifice that provides the proper flow rate for the desired particle size cutoff, and a vacuum pump. The flow rate is monitored by two independent gauges. The $PM_{2.5}$ samples in Underhill, VT, were collected on Teflon filters using module A of the sampler routinely employed in the IMPROVE network. Filters were subsequently analyzed

* Corresponding author e-mail: hopkepk@clarkson.edu; phone: (315)268-3861; fax: (315)268-6654.

10.1021/es0105865 CCC: $20.00
Published on Web 11/02/2001

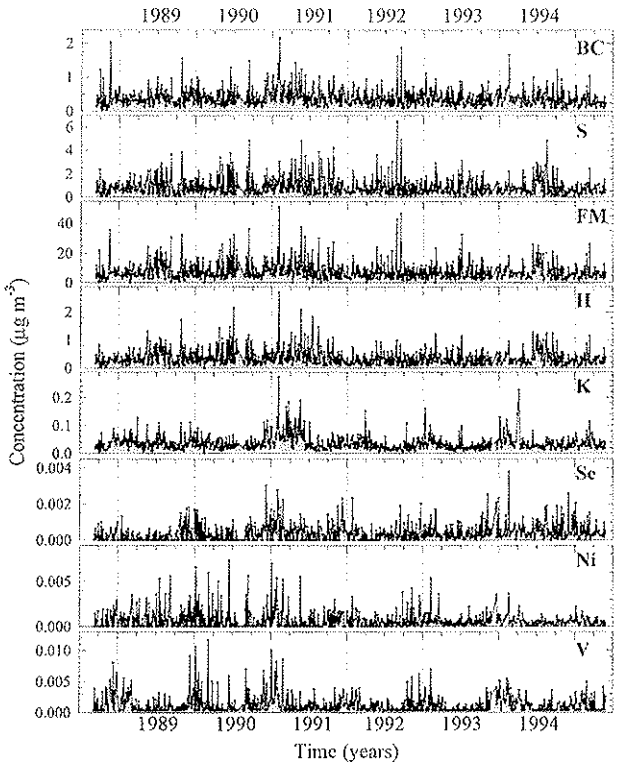

FIGURE 1. Comparison of the BC, S, FM, H, K, Se, Ni, and V concentration–time series for Underhill, VT. Data below the limit of detection were replaced by halves of the average detection limit values.

at the Crocker Nuclear Laboratory, Univversity of California, Davis (IMPROVE analytical laboratory) for mass (gravimetric), light absorption (B_{abs}, by laser integrating plate, LIPM) (*6*), elemental hydrogen (by proton elastic scattering analysis, PESA), and multiple elements with molecular weights ranging from Na through Pb (initially by proton induced X-ray emission, PIXE, and starting June 1992, by a combination of PIXE and X-ray fluorescence, XRF) (*5*, *6*). The addition of XRF affected the precision and minimum detectable limits for the measured elemental concentrations.

It was assumed for the black carbon mass concentration calculations that the absorption cross-section for BC aerosol is equal to 25 $m^2 g^{-1}$. This value is much higher than is typically employed (*8*), but this relationship was obtained between light absorption coefficient and EC at two nearby sites in the NESCAUM network where direct measurements of EC and absorption coefficient were conducted concurrently with the Underhill, VT, measurements. There are occasional "missing data" (no reported measurement) for one or more species (most often mass or B_{abs}) in 16 of the 853 daily samples.

Results

Initial Data Investigations. The time series of major aerosol species concentrations for Underhill, VT, are shown in Figures 1–4. Table 1 shows geometric means along with geometric standard deviations for the aerosol species measured in Vermont. For the below detection limit data, half of the detection limit values were used for the calculations. The percentage of observations with reported concentrations below the detection limit is also shown Table 1. Examples of scatterplots for the measured aerosol species concentrations are shown in Figures 5 and 6. Two different symbols represent the data for the season from October to April (winter) and from May to September (summer), respectively, reflecting the annual cycles in the time series of different species shown in Figures 1–4.

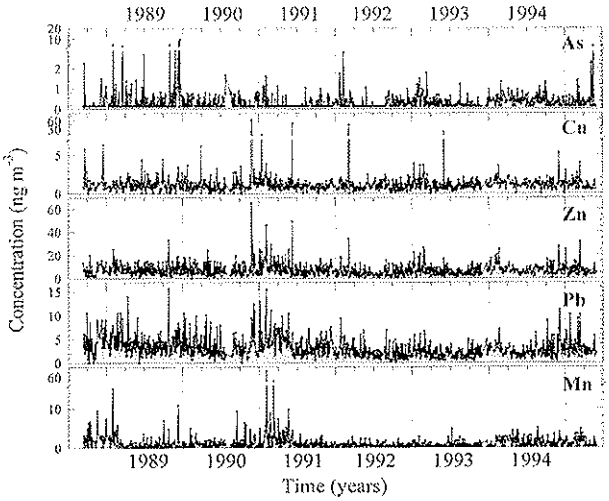

FIGURE 2. Comparison of the As, Cu, Zn, Pb, and Mn concentration–time series for Underhill, VT. Data below the limit of detection were replaced by halves of the average detection limit values.

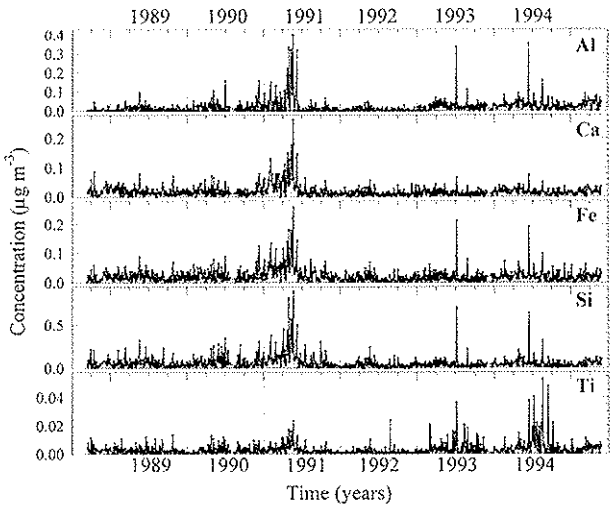

FIGURE 3. Comparison of the Al, Ca, Fe, Si, and Ti concentration–time series for Underhill, VT. Data below the limit of detection were replaced by halves of the average detection limit values.

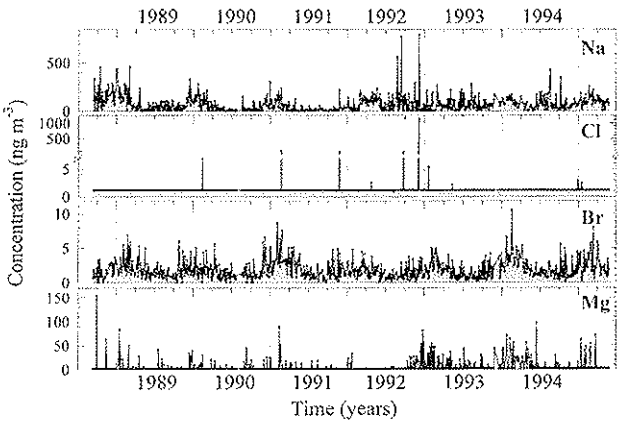

FIGURE 4. Comparison of the Na, Br, Cl, and Mg concentration–time series for Underhill, VT. Data below the limit of detection were replaced by halves of the average detection limit values.

A study of the time series and the scatterplots is a useful tool of data analysis. It provides a helpful preliminary understanding of the possible sources of aerosol. The discussion below depends on several assumptions regarding

TABLE 1. Geometric Means (GM),[a] Geometric Standard Deviations (GSTD), Percentage of Data below Detection Limits (BDL), and Coefficients *a* and *b* That Were Used for the PMF Error Estimate Calculations

elements	GM (ng m^{-3})	GSTD	BDL (%)	*a*	*b*
Al	8.33	4.42	35.5	1/16	4
As	0.23	2.46	51.2	1/49	1
BC	358	1.73	0.0	1/4	1
Br	1.49	2.15	1.6	4	4
Ca	15.1	2.31	0.9	1600	16
Cl	0.97	1.64	98.7	1/49	9
Cr	0.35	1.77	75.5	1	1
Cu	0.99	2.03	2.7	1	1
Fe	17.1	2.39	0.0	100	1
H	309	2.03	0.2	100	1
K	31.7	1.85	0.1	50/8	1/64
Mg	3.46	2.58	79.4	1	100
Mn	0.75	2.70	34.1	9/4	9/4
Mo	0.58	1.41	97.7	1	1
Na	42.1	3.24	19.9	3	2
Ni	0.39	3.36	31.7	1	1
P	0.94	1.45	99.3	1	1
Pb	2.69	1.95	0.5	16	1
Rb	0.13	2.26	77.0	1	1
S	702	2.23	0.0	16	1
Se	0.28	2.72	28.0	1/16	1
Si	44.1	2.63	1.4	1600	1
Sr	0.18	1.85	72.7	1	1
Ti	2.02	2.88	15.4	16	1
V	0.82	2.51	41.6	1	1
Zn	6.12	1.96	0.1	2	1
Zr	0.23	2.05	88.6	1	1
FM	6398	2.16	1.3		

[a] Data below the limit of detection were replaced by half of the reported detection limit values for the geometric mean and the geometric standard deviation calculations.

the probable sources of aerosol. These assumptions will be further checked by using a more sophisticated analysis, PMF. The results of the PMF analysis are presented at the end of this section.

Figure 1 shows a time series of the total fine mass (FM) concentration and concentrations of elements that mainly represent different combustion sources. Aerosol BC and S concentrations ranged from 0.05 to 2.2 μg m^{-3} and from 0.01 to 6.5 μg m^{-3}, respectively, while the total fine aerosol mass concentration ranged from 0.2 to 51.1 μg m^{-3} (Figure 1). The H and S time series are similar, having maxima in summer and minima in winter. The summer increase in S is due in part to enhanced secondary sulfate formation. The summer peak in H is also likely to be related to increased sulfate production and also to secondary organic carbon production.

No clear structure can be seen in the seasonal variations of black carbon. Several high pollution episodes (e.g., during the summer of 1992) can be seen simultaneously in the BC, S, and FM time series (Figure 1). However, other black carbon peaks (e.g., during winter 1991) are correlated well with FM, K, and H but not with S, suggesting the presence of woodsmoke particles with a high organic matter (non-sulfate hydrogen) content.

Figure 5A shows a BC/S scatterplot. A slope for the winter linear regression fit is larger than for the summer fit while the correlation coefficient is higher for the summer. Emissions with the high BC/S ratio generally represent wood burning (*9*) as well as exhaust from motor vehicles (*9*) and incineration (*10*). To illustrate the relationships between BC and S observed in earlier studies of specific source emission compositions, lines are provided in the figure with slopes based on the data provided by Watson et al. (*9*) and Olmez et al. (*10*). The coal plant reported by Olmez et al. (*10*) is the only coal plant in the EPA source profile library with any measurements of EC and OC, but there is no basis to know how representative this measurement is of the broad category of eastern and midwestern coal-fired power plants. The described properties of the BC and S time series and the corresponding scatterplot suggest that multiple sources including a combination of local and distant sources of S and BC dominate during the winter season. Therefore, the BC/S ratio is not stable in the winter season, and the BC–S correlation is low. In contrast, the aerosol in the summer is transported from distant sources. It is likely to be better mixed during transport (high BC–S correlation), and the S/BC ratio is higher during the summer because of photochemically enhanced sulfate production from SO_2 during transport. The dotted lines represent the PMF factor loading ratios, which will be described below.

Both the FM/S and FM/BC scatterplots show higher correlations for the summer subset of points than for the winter (Figure 5B,C). These plots also suggest that it is likely that several sources produce aerosol with different FM/BC and FM/S ratios during the winter season while aerosol BC and S content in the summer is more stable. Black carbon contribution to the total fine mass is higher during the winter season so that the BC/FM ratio is higher for the winter subset of points in Figure 5B. In contrast, sulfur contribution to the total fine mass is about the same during the winter and summer seasons so that the slopes for the linear regression fits for the summer and winter subsets are about the same (Figure 5C).

The K, Se, Ni, and V time series have maxima in the winter and spring season and minima in the summer (Figure 1). This result could be due to higher emission rates in the winter and/or the seasonality in the synoptical conditions in the area of sampling that determines the pollutant transport. Ni and V usually represent particles emitted from oil-fired power plants (*10*). Concentrations of Ni and V show negative trends over the sampled time interval (Figure 1), which could indicate a reduction in the oil-fired power plant emissions. No clear trends for other elements can be seen (Figures 1-4).

Figure 5D shows a Se/S scatterplot. Se is generally an important tracer for coal combustion (*10*). The slope for the linear regression for the winter subset of the data points is higher than that for the summer data while the corresponding correlation coefficient is higher for the summer. The summer S/Se ratio is close to the ratio obtained for emissions from an oil-fired power plant (*10*) (Figure 5D). This result could be due to either a higher contribution from the oil combustion sources or the greater production of secondary sulfate during the summer season. However, lower concentrations of V and Ni in the summer indicate a lower contribution from oil-fired power plants. In addition, the V/Ni scatterplot (Figure 6A) shows a lower correlation for the summer subset and a higher Ni/V ratio. Thus, it is likely that secondary aerosol formation from SO_2 is the dominant cause of the observed relationships.

Figure 2 shows the time series plots of the As, Cu, Zn, Pb, and Mn concentrations. These elements usually represent nonferrous smelting, incineration, and motor vehicle emissions. There is a good correspondence between Cu, Zn, and Pb time series. However, there are some differences (e.g., peaks in Pb concentration but low Cu, Zn, and Mn values in the spring–summer of 1992) that indicate emissions from multiple sources.

The Zn/Pb and Zn/Cu scatterplots are shown in Figure 6A. The slopes for the Zn/Pb summer and winter subsets are equal and close to the slope obtained for the emissions from a municipal incinerator (*10*). However, Zn–Pb correlation coefficients are relatively low, meaning that there are other

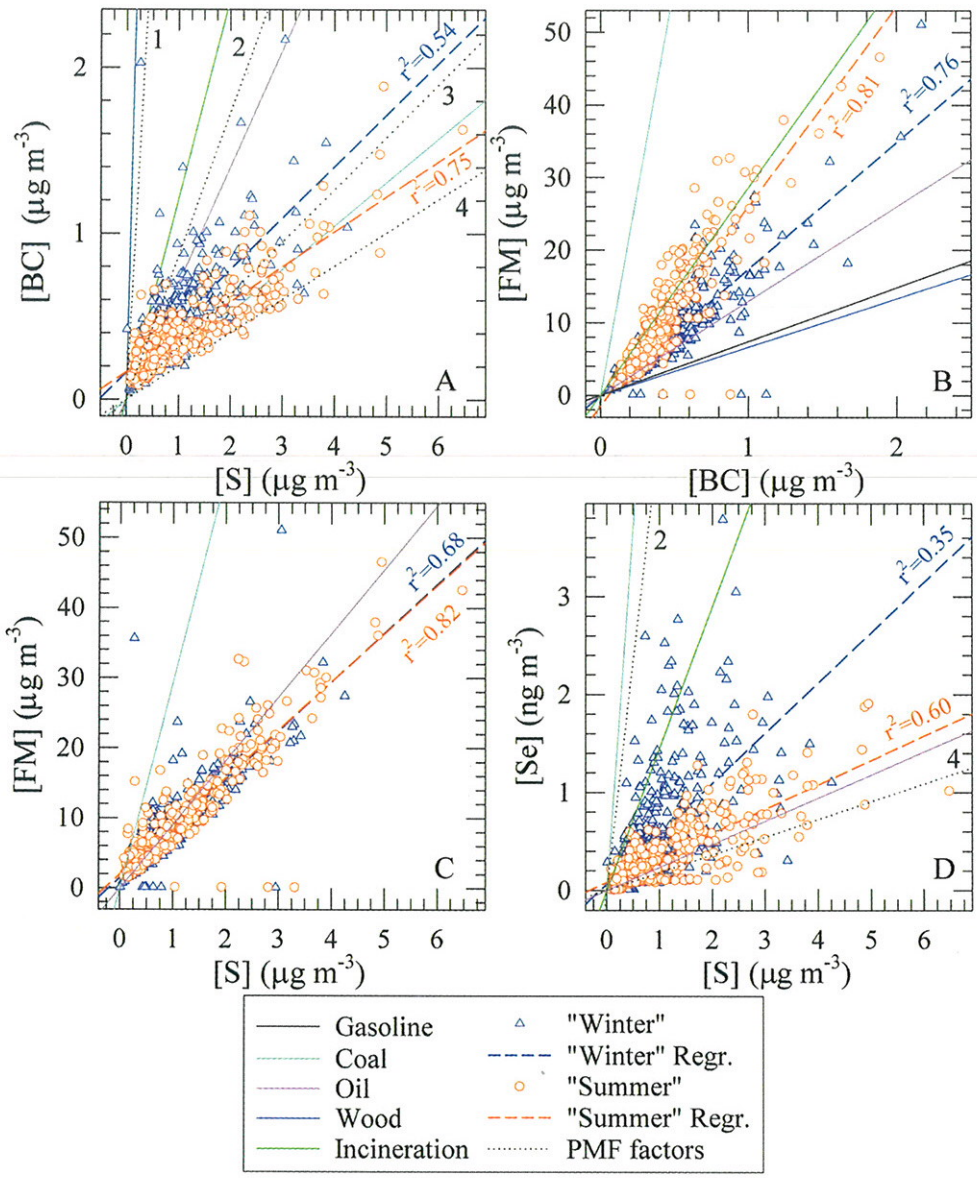

FIGURE 5. Concentrations of black carbon (BC) vs S (A), fine mass (FM) vs BC (B) and S (C), and Se vs S (D). Dashed lines represent linear regression fits for the winter and summer groups of points. The solid lines show ratios of element concentrations measured in aerosol emitted from different sources (*9, 10*). The dotted lines with the numbers represent ratios of loadings for the corresponding PMF factors.

possible sources of Pb and/or Zn. Indeed, the Zn/Cu scatterplot shows two separate groups of data points (Figure 6C). One with a high Zn/Cu ratio may represent emissions from incineration or zinc smelting. The other subset with a lower Zn/Cu ratio could indicate emissions from other sources such as copper smelting.

Figure 3 shows the time series for soil elements, Al, Ca, Fe, Si, and Ti. There is a good correspondence between the time series showing a likely common source for these species. The only major difference between the time series is the relatively low Ti concentration during the spring–summer of 1991. Figure 6D shows the Al/Si scatterplot. Coal combustion could be another source of Al and Si (*10*). The lower correlation for the winter subset could be related to relatively small variations and low absolute values of both Si and Al during the winter time (Figures 3 and 6D). About 35% aluminum values are below the limit of detection (Table 1). These data points were replaced by half of the reported detection limits. These points can be seen in the Al/Si scatterplot (Figure 6D) and raise doubts about the reported MDL for Al in these data. The Al/Si ratio for the points where Al was above the MDL is substantially higher than Mason's global average estimate for the earth's crust (*11*). The observed ratio is consistent with other fine particle measurement data such as those observed by Cooper et al. (*12*), who reported a composite Al/Si ratio of 0.47 from multiple fine particle sources in California.

Finally, time series for elements that usually represent sea salt aerosol are shown in Figure 4. Only very few Cl values have been measured, and about 99% of data is below the limit of the detection (Table 1). Cl peaks usually correspond to Na peaks, indicating a common source of Cl and Na (Figure 4). The Br time series indicates a clear seasonal pattern with higher concentrations in winter. The Na and Br time series are similar during the period from 1989 to 1991 (Figure 4). However, the Na time series for the period from 1992 to 1994 correspond better to the S series shown in Figure 1. Sea salt transported to Underhill could be expected to have taken sufficient time that it would have been subjected to displacement of halides by sulfuric and/or nitric acid. In addition to the sea salt aerosol, Br could also be present because of emissions from other sources such as municipal waste

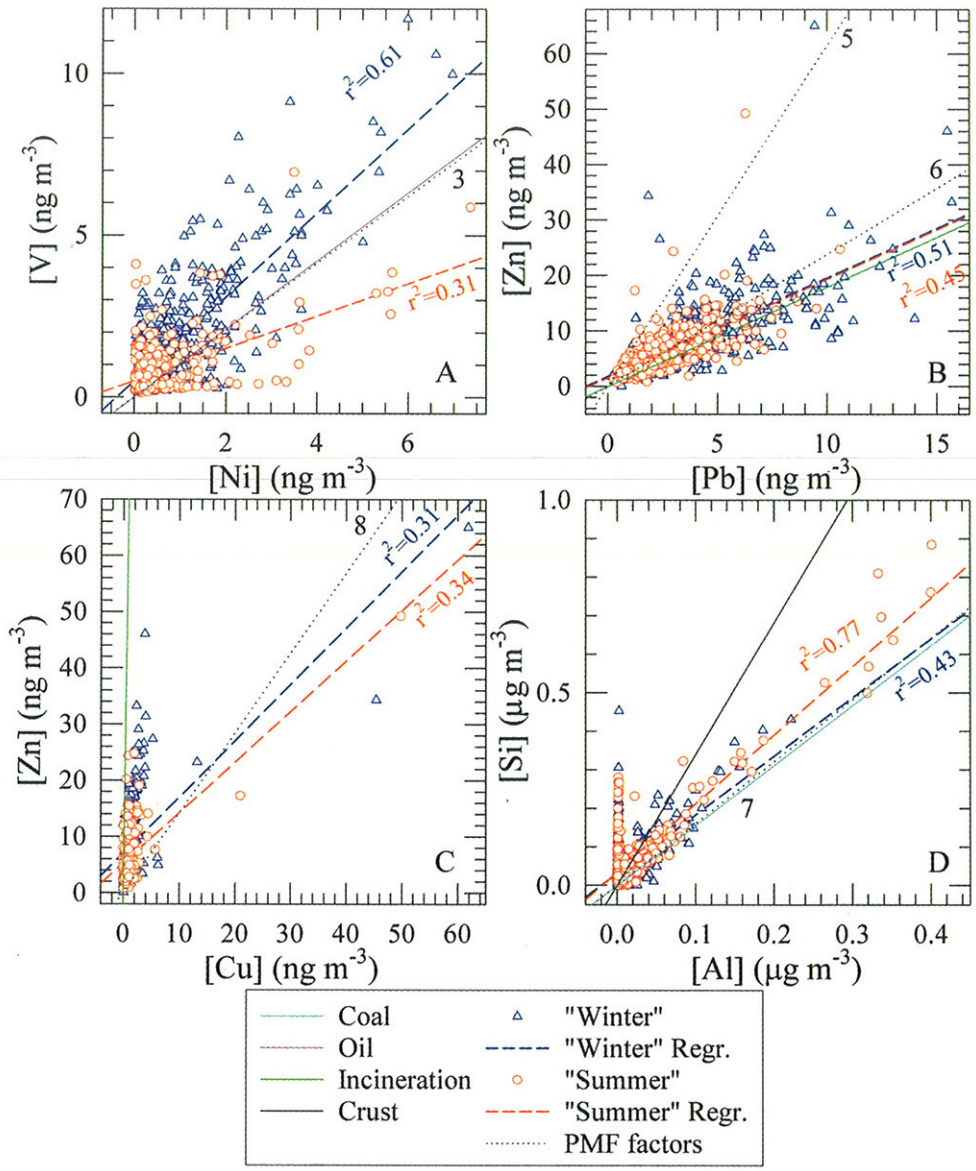

FIGURE 6. Concentrations of V vs Ni (A), Zn vs Pb (B), Zn vs Cu (C), and Si vs Al (D). The dashed lines represent linear regression fits for the winter and summer groups of points. The solid lines show ratios of element concentrations measured in aerosol emitted from different sources (*9*–*11*). The dotted lines with the numbers represent ratios of loadings for the corresponding PMF factors.

incineration (*10*). These data support this conclusion because the Br time series does not track well with the Na and Cl time series.

It can be seen that an analysis of the time series and the scatterplots above provides some qualitative understanding of the experimental data and indicate possible sources of aerosol. The assignments of possible aerosol sources were further studied with the PMF analysis.

Positive Matrix Factorization. A new type of factor analysis, PMF (*3*), utilizes error estimates of the data to provide an optimum data point scaling. PMF is a method based on solving the factor analysis problem by least-squares using a data point weighing method (*13*). The solution was forced to be nonnegative through the use of a penalty function.

The factor analysis model is given by

$$\mathbf{X} = \mathbf{G} \times \mathbf{F} + \mathbf{E} \tag{1}$$

where **X** is a matrix of observed data, **G** is the unknown left-hand factor matrix, **F** is the unknown right-hand factor matrix, and **E** is a matrix of residuals. The difference between the model and the data is

$$\mathbf{E} = \mathbf{X} - \mathbf{G} \times \mathbf{F} \tag{2}$$

The least-squares problem can then be posed as

$$\min_{\mathbf{G},\mathbf{F}} Q(\mathbf{X},\sigma,\mathbf{G},\mathbf{F}) \tag{3}$$

where

$$Q = \left|\left|\frac{(\mathbf{X} - \mathbf{GF})}{\sigma}\right|\right|^2_{\mathrm{F,G}} = \sum_i \sum_j \left(\frac{e_{ij}}{\sigma_{ij}}\right)^2 \tag{4}$$

with

$$e_{ij} = x_{ij} - \sum_{k=1}^{p} g_{ij} f_{ij} \tag{5}$$

and σ is a known estimated uncertainty for each x_{ij} value. The details of the algorithm are provided by Paatero (*13*).

The important advantage of the PMF method is the ability to handle missing and below detection limits data by adjusting the corresponding error estimates of these data points. It was especially essential for the Vermont data set because data for some elements such as Cl have over 90% of the values below limits of detection (Figure 4, Table 1). Missing data and data below detection limits values were replaced by mean concentration and half of the detection limit values, respectively, and large error estimates were used for such values. Only BC data had a very few missing values. PMF error estimates equal to 25 times the mean values were used for such data points. For the determined values, one should specify the effective error estimates so that they include all errors that produce a deviation between the fit and the observed value.

The following formula was used for the PMF error estimates:

$$\sigma_{ij} = \sqrt{a_j u_{ij}^2 + b_j d_{ij}^2} \qquad (6)$$

where u_{ij} and d_{ij} are the analytical uncertainty and the analytical detection limit, respectively, for sample i and element j; a_j and b_j represent scaling factors for the PMF weights for each element j from the original data set. The uncertainty u_{ij} for the below the limit of detection data was equal to zero so that only the second part of the formula was used for such data points. The set of values of the coefficients is presented in Table 1.

There is no simple rule for calculating error estimates. Analytical errors are only part of the total random error which is unknown. Data for some elements such as Cl, Al, Mg, etc. had a large number of the values below detection limits. In addition, Al and Cl appear to have unrealistically low values when the values below limits of detection were replaced by half of the detection limits because both Al and Si, and Cl and Na, represent the same two sources, soil particles and sea salt, respectively. Therefore, it is hard to understand a presence of the points with extremely high Si/Al ratio in Figure 6D. For this reason, some of the soil and sea salt elements were downweighted to obtain more realistic input data. Si and Ca data were downweighted by using larger error estimates for them (high a values, Table 1). In addition, the data below the detection limit for Al and Cl were downweighted (higher b value in eq 6), and at the same time, higher weights for the detected values for Al and Cl were used (lower a) (Table 1). Lower error estimates for soil elements resulted in separate factors for Al and Si, which appears to be unrealistic.

A similar approach of the adjustments of the error estimates was used also for the As and Se data. Data for As and Se have about 51% and 28% of values below the detection limits, respectively. The weights for the detected data for As and Se have been increased (lower a) (Table 1).

It was possible to obtain main factors without this adjustment of error estimates, but in most cases higher weights for the measured data and lower weights for the below the detection limit data result in source profiles with more realistic loading ratios. The factor loadings were compared with known ratios of loadings for different sources (*9*–*11*).

Thus, in contrast to our previous work (*14*), where the same linear combination of the detection limit and uncertainty or the same single formula was used for all the elements, different weights for different elements were used in this study. This approach, despite its subjectivity in the method of weighting the data, improved the resolution of the PMF model so that 11 sources of aerosol were identified. In addition, more realistic chemical composition of the factors associated with elements that have large number of data below detection limits was obtained. A unique linear combination formula for the error estimates resulted in poor representation of soil and sea salt aerosol, the species that has elements with a large number of data below detection limits. A similar approach to weighting the data was applied to major ion compositions data from daily precipitation samples collected at a number of sites in Finland (*15*), and considerable information on the sources of these ions was obtained through the use of PMF.

The final set of values of the error estimates was obtained by running the PMF program many times with different sets of error estimates and applying the trial and error method until a substantially improved fit to the data was achieved. The quality of the model was evaluated by the analysis of the Q values, the loading ratios for the sea salt and soil factors, the frequency distributions of the residuals, and the results of the multiple linear regression calculation of the reconstructed fine mass concentrations. About 130 combinations of weight coefficients were tested for solutions with a different number of factors, and the final set of a and b parameters is presented in Table 1.

The nonnegativity requirement in PMF analysis decreases the rotational freedom, and in some cases, the result is unique with no rotational freedom. In the present study, the amount of rotation freedom was very limited.

Eleven factors were obtained for the data set from Vermont (Figures 7 and 8). The theoretical value Q is approximately equal to the number of degrees of freedom or the number of input data points minus the number of the solution values. The theoretical Q was equal to 13 351 while the Q value for the obtained 11-factor solution was equal to 5367. A lower Q value could indicate the higher values of the input error estimates. These higher error estimates were mainly used for soil and sea salt elements (Table 1). They improved the source profiles obtained but reduced the final Q value. Therefore, this difference between theoretical and obtained Q values appears to be reasonable.

The solution was normalized by using fine mass concentration data and weighted multiple linear regression (*16*). It was assumed that a linear combination of factor concentrations is equal to measured total fine mass concentration. The constant of the linear regression was assumed to be zero. This normalization also provided an additional test of the PMF model and the correctness of the number of factors that have been chosen for the solution for each data set. An unrealistic number of factors for the PMF model very often result in negative values for the regression coefficients. The squared correlation coefficient, r^2, was equal to 0.97. As a result of such normalization, the time series G for factors has units of mass concentration (μg m^{-3}) (Figure 7). The source profiles, F, have units of parts per million (Figure 8). PMF produces errors for the output values. The loading error bars shown in Figure 8 were obtained by propagation of these PMF errors and the errors of the multiple regression coefficients.

Results of the PMF analysis are presented in Figures 7 and 8. The first woodsmoke factor has high loadings of BC, H, and K (Figure 8, factor 1). This factor is attributed to particles from local wood smoke and possibly from other related combustion sources. The ratio of the BC to S loadings for the woodsmoke factor corresponds well to a reported ratio for wood combustion (*9*) (Figure 5A, line 1). The time series for the woodsmoke factor has a maxima in the winter/spring season and minima in the summer (Figure 7, factor 1) representing higher emissions of wood smoke or/and more effective transport of soot from sources to the sampling site in winter. The time series also shows several high spikes during summers, indicating smoke from several forest fires

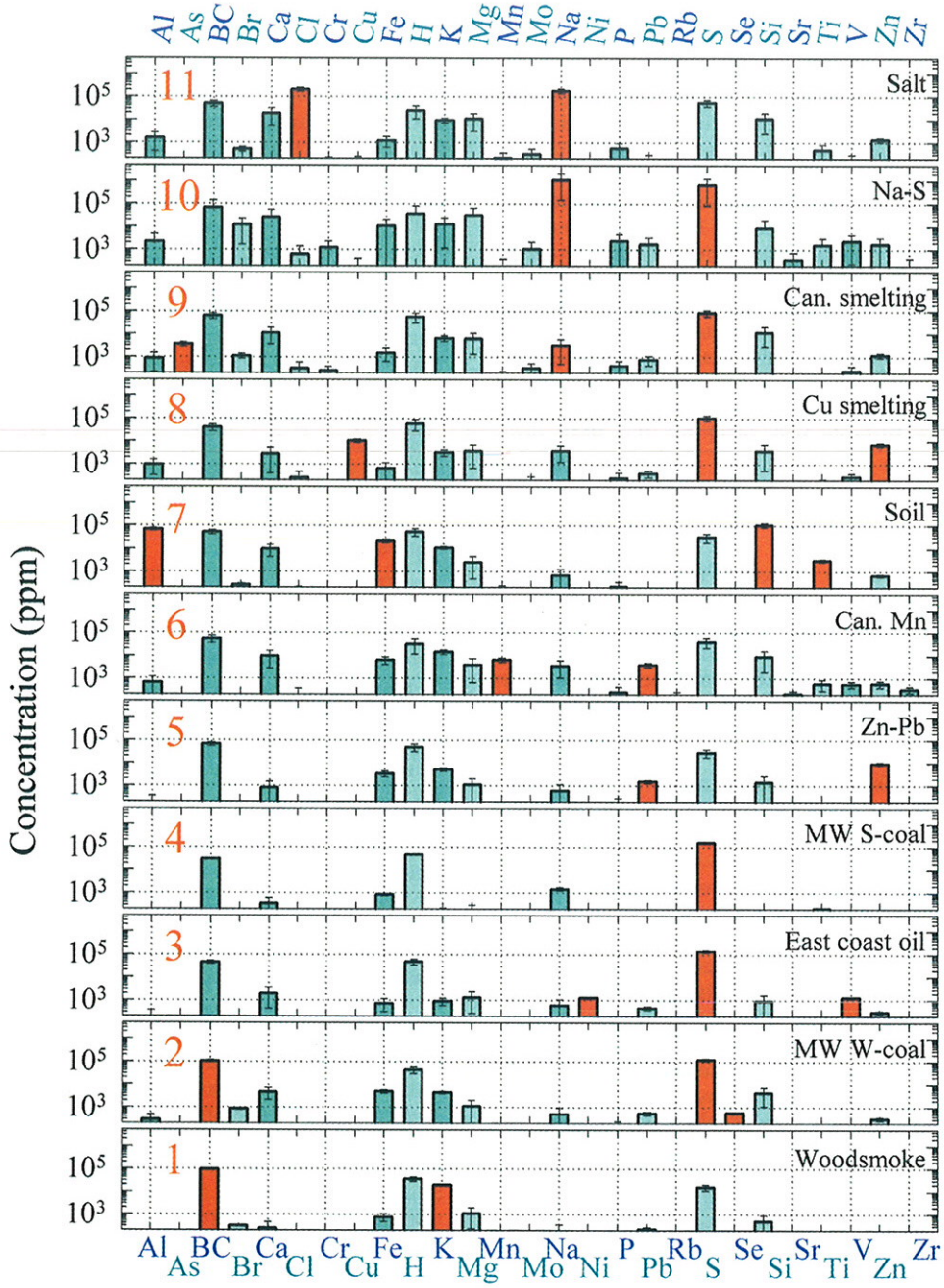

FIGURE 7. Temporal variations of factors obtained by the PMF for Underhill, VT. The weighted multiple regression was used for the time series normalization.

that were known to have occurred in Quebec. Fireworks around the fourth of July can also be observed (Figure 7, factor 1).

Two factors with the highest loadings of S have been obtained (Figures 7 and 8, factors 2 and 4). They also have high loadings of BC and H. In addition, the first S factor also has the highest loadings of Se (Figure 8, factor 2), suggesting emissions from coal-fired power plants. S/Se ratio was equal to 214 for the first S factor, which is close to 136, a reported S/Se ratio for coal-fired power plant emissions (*10*) (Figure 5D, line 2). However, as displayed in Figure 5A, line 2, the BC/S ratio for this factor was higher than the reported BC/S ratio for a coal-fired power plant (*10*) (Figure 5A, line 2). There are quite limited data on source profiles in the eastern United States so that it is not clear if these values reflect the average emissions from multiple plants that impact the Underhill site or if there are contributions from other sulfur-producing combustion sources with co-emission of black carbon. It is also possible for the factor analysis to overly apportion BC to this factor. The factor has an annual cycle with maxima during the winter/spring season and minima in the summer (W-Coal) (Figure 7, factor 2). The presence of Si and Fe loadings in the first S factor (Figure 8, factor 2) could arise from Si emissions from coal combustion sources (*10*). It will be shown below that this source is largely associated with transport from the midwestern United States and so will be denoted as MW winter coal.

The second S factor has the opposite annual cycle with the summer maxima (Figure 7, factor 4). The S/Se and S/BC ratios were higher for the second S factor than reported ratios for coal-fired power plant emissions (*10*) (Figure 5A,D, line 4). This change in ratio is likely in part related to more effective

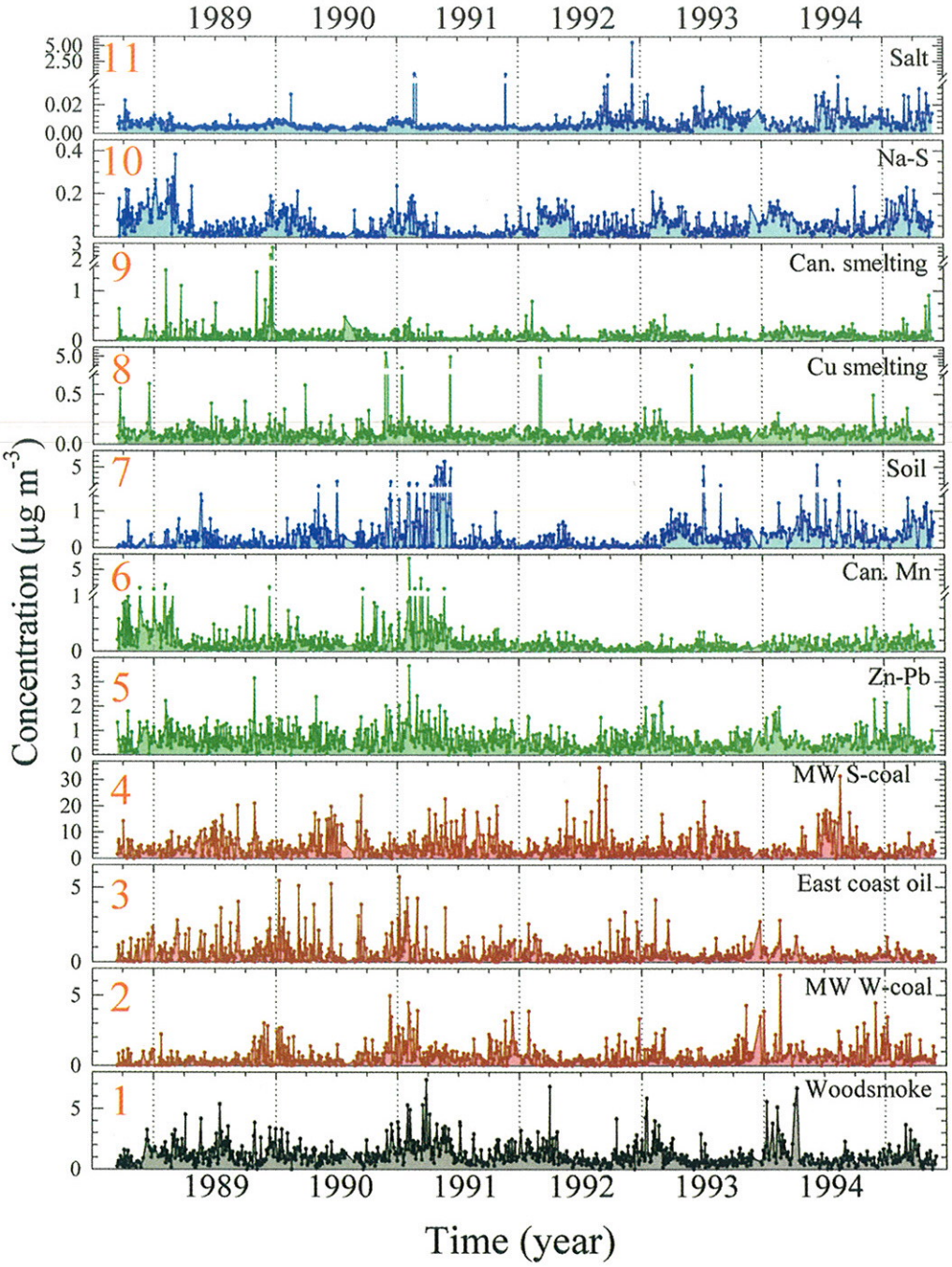

FIGURE 8. Source profiles of aerosol species in the factors obtained by the PMF for Underhill, VT. Red bars represent the highest loadings. Error bars were obtained by the propagation of the errors calculated by PMF.

secondary sulfate production from SO_2 in the summer. The ratios also were close to slopes for the linear regression fits for the summer groups of original data points (Figure 5A,D, line 4). It is suggested that the second S factor represents the photochemically enhanced sulfate production from SO_2 in the summer (MW summer coal). There could also be secondary sulfate production from heterogeneous processes in cloudwater and fog. Sources related to the second S factor provide the highest fine particulate matter mass concentrations (Figure 7, factor 4). It is likely that the two S factors basically represent the same coal-fired power plants with the differences between the factors representing the extremes of photochemical production of sulfate from the emitted SO_2. It will be shown below that these two coal combustion factors represent emissions from mostly common source areas extending from the lower Great Lakes to the south of the Ohio River Valley, encompassing the locations of many large electricity-generating plants and industrial sources in the Midwest.

Another combustion factor along with high BC, S, and H loadings has the highest loadings of V and Ni (Figure 8, factor 3). This factor is suggested to represent emissions from oil-fired power plants located along the east coast of the United States. The Ni/V ratio was equal to 0.97 for this factor and it is close to 0.95, a reported ratio for an oil-fired power plant (*10*) (Figure 6A, line 3). However, the S/BC ratio is higher than the oil combustion ratio (*10*) (Figure 5A, line 3). This difference is consistent with additional sulfate production en route from the source region to northern Vermont. Higher concentrations during winter/spring for the oil factor are

observed (Figure 7, factor 3). Concentrations for this factor show a significant negative trend over the sampled time interval. A weighted linear regression was used to calculate the trend in the oil factor concentration expressed on a logarithmic scale. The squared correlation coefficient for the fit was statistically significant and equal to 0.21. The trend in the oil combustion factor concentrations is equal to $-5.5 \pm 0.5\%\ yr^{-1}$. This negative trend suggests a reduction in oil-fired power plant emissions during the period from 1988 to 1995.

The PMF solution contained a factor with high loadings of Zn, Pb, H, BC, and S (Figure 8, factor 5). The high Zn, Pb, and BC loadings for the factor could arise from several types of sources. Possible source types include municipal waste incineration and nonferrous metal smelting. The Zn/Pb ratio was equal to 6.1 for this factor which is about 3.5 times higher than the 1.8 ratio reported for municipal incinerator emissions (*10*) (Figure 6B, line 5). This ratio represents older emission measurements when leaded solder was still in use in food containers. Such use terminated in the late 1980s. However, the distribution of source areas across the upper Midwest described below would suggest a mixture of sources contributing to this factor. The time series for the Zn−Pb factor had maxima during the winter/spring season and had minima in the summer (Figure 7, factor 5).

The PMF solution for the Vermont data set contained a factor with high loadings of Pb, BC, H, Mn, and Br (Figure 8, factor 6). This factor may represent emissions primarily from motor vehicles. The ratio Mn/Pb is equal to 1.7, which is higher than the 0.7 ratio reported for recent U.S. motor vehicle emissions (*9*). This difference may indicate that in addition to emissions from motor vehicles there could be some other sources, most likely Mn smelting in Canada, related to this factor. Thus, this factor will be denoted as Canadian Mn. This factor could indicate the influence of Canadian motor vehicles, burning gasoline with a uniquely Canadian Mn additive (methylcyclopentadienyl manganese tricarbonyl or MMT). The Mn factor had also high loadings of BC, Si, and other soil elements, suggesting the mixing of smoke from motor vehicles and road dust during transport. In addition, a large Mn alloy production plant southwest of Montreal in Beauharmois, PQ, may have also been an important Mn source during the first several years of this sampling period (*17*). It could also be associated with emissions from the numerous iron and steel industries of the Midwest (*18*).

As displayed in Figure 5B of the scatterplot of zinc against lead, the Canadian Mn factor (line 6) describes the main group of data points while the Zn−Pb factor (line 5) is related to a set of a smaller separate group of points with a higher Zn/Pb ratio. These lines illustrate how the two factors correspond to distinct features in the raw data.

The soil factor has the highest loading for Al and Si (Figure 8, factor 7). This factor had also high loadings of BC, Ca, Fe, H, K, and Ti (Figure 8). The high loadings of BC could be connected with the possible contribution of the soil fraction to the measured aerosol optical absorption coefficient. The ratio Al/Si for the soil factor was equal to 0.62. This ratio was about 2 times higher than in the average earth crust (0.293) (*11*) (Figure 6D, line 7). However, this value agrees well with the properties of original data: the slopes for the linear regression fits for the Si/Al scatterplot are also lower than the average crust Si/Al ratio (Figure 6D). The soil factor also had low loadings of S. This result could reflect mixing of anthropogenic particles and dust during transport and/or possible emission of Si and Al from coal combustion sources resulting in the increase in Al/Si ratio. The time variations of the soil factor have peaks in the summer that corresponds to the likely higher rates of soil entrainment in the summer (Figure 7, factor 7). An episode of high soil concentrations during the spring/summer of 1991 is most likely related to local construction activity near the Underhill sampling site. It is likely that both local and long distance sources of soil aerosol are related to the soil factor.

The second factor with high loading of Zn also has the highest loadings of Cu (Figure 8, factor 8). The time series of the Cu factor represent Cu−Zn peaks observed in the Cu original data time series (Figure 2). This factor may indicate emissions from some aperiodic smelting of nonferrous metal ores and will be denoted as Cu smelting. However, the time series follows the Cu time series with a limited number of spikes. There is a good correspondence between the Zn/Cu loading ratio for this factor and the original data linear regression fits representing a group of points with the high Cu/Zn ratio (Figure 6C, line 8).

A factor with the highest loadings of As and S has been identified by PMF (Figure 8, factor 9). It may indicate transport from a large smelter located near Noranda at the Quebec/Ontario border (*17*). It is identified as a Canadian smelter factor. No clear structure of an annual cycle in the seasonal variations for both Mn and As factors is observed (Figure 7, factors 8 and 9).

The salt factor has high loadings of Ca, Cl, H, K, Mg, Na, and S (Figure 8, factor 11). The Na−S factor has high Na but low Cl loadings (Figure 8, factor 10). Higher errors were obtained for the Na−S factor loadings (Figures 8). The presence of the Mg and K suggests sea salt with a contribution from generation of a salt aerosol from the road salting during winters. The presence of BC and Si supports the influence of roads and local sources. This factor was obtained despite the large number of below detection limit values for Cl concentrations (Table 1). However, given the location of the sampling site, it is unlikely that marine aerosol can reach Underhill without significant atmospheric processing. Cl/Na loading ratios for the salt factor and for the seawater are 1.16 and 1.80, respectively. The ratio Cl/Na for the salt factor was lower while the ratio S/Na was higher (0.31) than in sea salt (0.08). Reaction with H_2SO_4 during the fine aerosol transport could produce the Cl deficit and excess of S in the salt factor.

The time series for the Na−S and salt factors had maxima in the winter/spring season and generally had minima in the summer (Figure 7, factors 10 and 11). Summer maxima for the salt factor in 1993 and 1994 correspond well to the summer coal factor time series that could indicate transport of marine aerosol from the Gulf of Mexico with substantial displacement reactions producing a mixture of sulfate and salt particles. There was also a possibility of a separation of the salt and Na−S factors associated with the presence of the large number of values below limits of detection for the concentration of Cl (Table 1). However, most likely the presence of these two factors for the data is the result of presence in the area of observations of several types of particles with the high loadings of Na.

Figure 9 presents a comparison of the reconstructed and measured fine mass concentrations. Figures 10−12 show mass contributions from different sources identified by PMF for the total sampling period (Figure 10) and for the periods from October to April (winter) (Figure 11) and from May to September (summer) (Figure 12).

The concentration of particles emitted from wood burning and coal-fired and oil-fired power plants were higher in the winter (Figures 9−12). The highest concentration of these three factors were obtained from December to March (Figure 9, factors 1−3). In contrast to this, the second S factor concentration is the highest in July and the lowest from November to January (Figure 9, factor 4). This indicates higher emissions and/or more effective transport during the winter season leading to higher contributions from the first three combustion sources, but the lower rate of photochemical

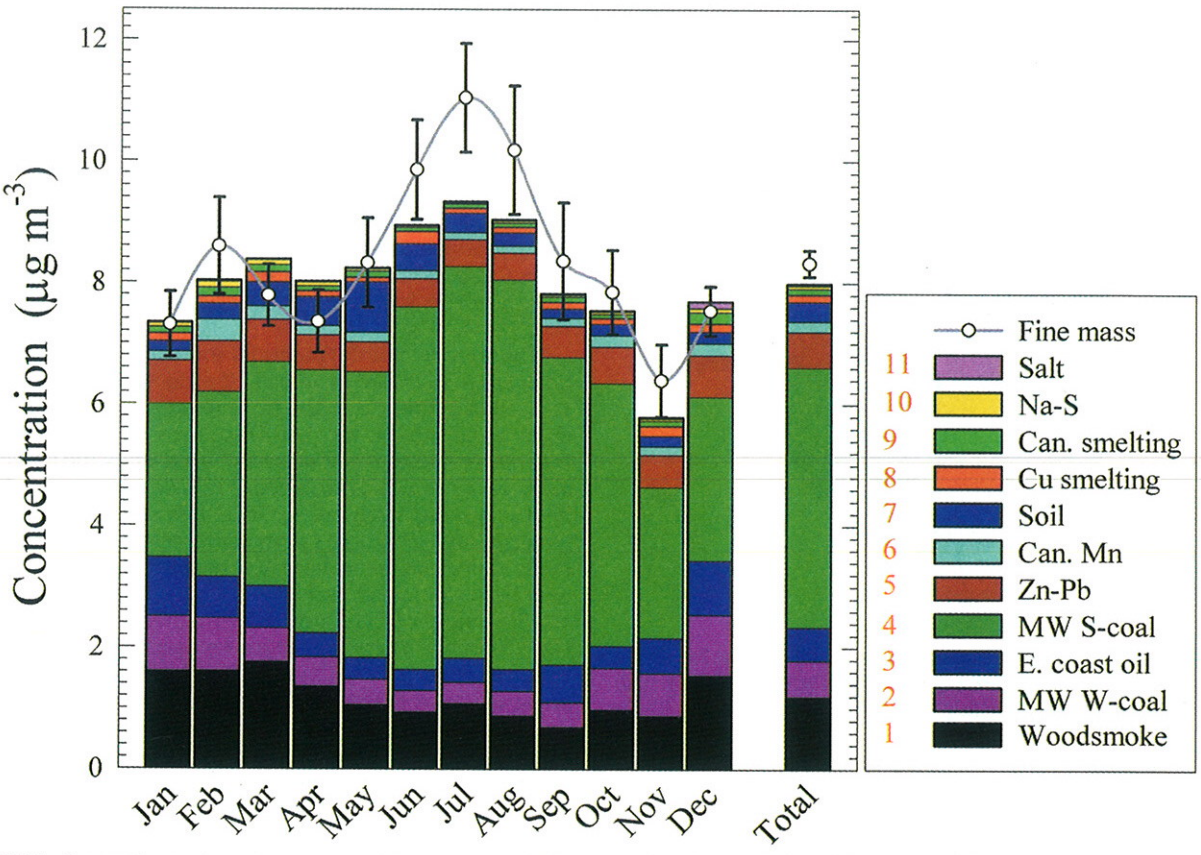

FIGURE 9. Comparison of monthly means of factor concentrations obtained by the PMF with measured fine mass concentration for Underhill, VT. Fine mass concentration error bars were calculated by a propagation of the reported analytical uncertainties.

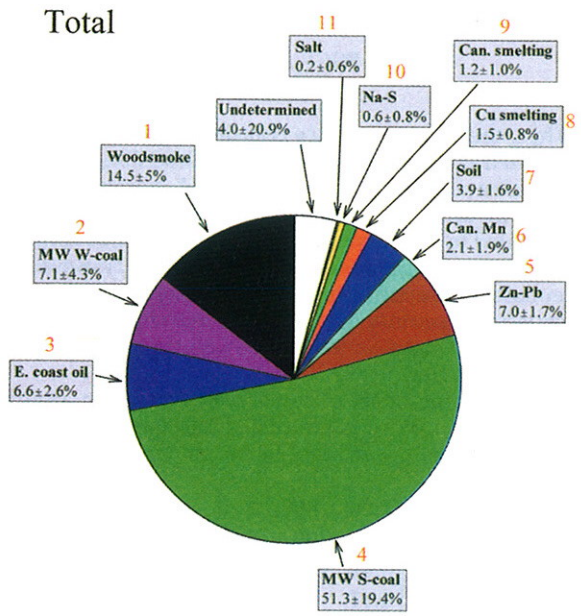

FIGURE 10. Average source contributions for the whole period of sampling obtained by the PMF for Underhill, VT. Red digits represent corresponding PMF factor numbers.

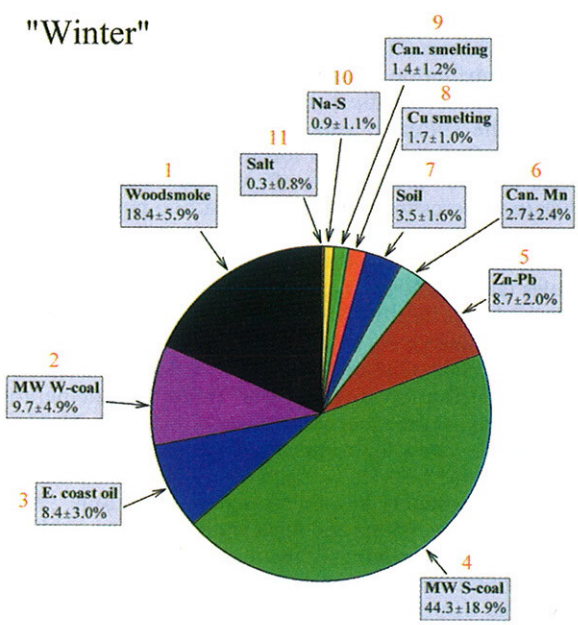

FIGURE 11. Average source contributions for the period from October to April (winter) obtained by the PMF for Underhill, VT. Red digits represent corresponding PMF factor numbers.

sulfate production during winter results in lower contribution from the summer S factor. Concentration of the summer S factor peaked in June–August because of the intensive secondary aerosol formation while the first three combustion factors show lower concentration because of lower emissions from the combustion sources during summer (Figure 9, factor 4). The three first combustion sources collectively accounted for about 28% of the total fine mass (Figure 10, factors 1–3), but their contribution is 2× higher in the winter (36%) (Figure 11, factors 1–3) than in the summer (18%) (Figure 12, factors 1–3). The contribution from the secondary aerosol S factor is approximately 51%. It is equal to 60% during the summer season and lower during winter (44%) (Figures 10–12, factor 4). The sum of the four combustion source contributions is approximately equal to 80% and about the same in the winter

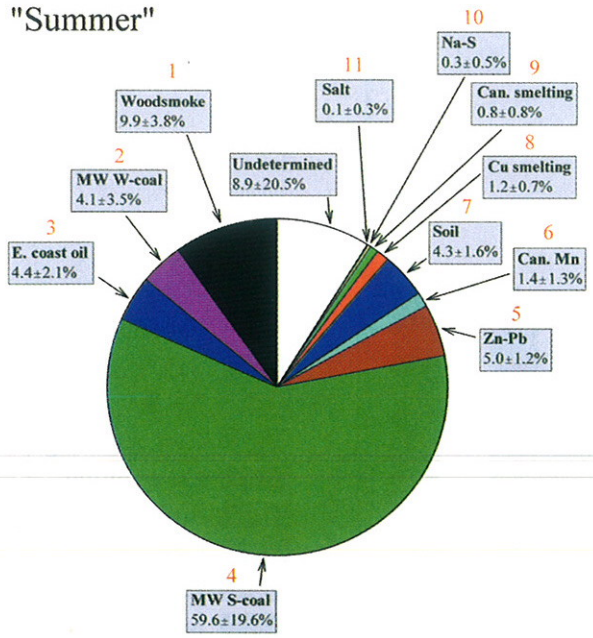

FIGURE 12. Average source contributions for the period from May to September (summer) obtained by the PMF for Underhill, VT. Red digits represent corresponding PMF factor numbers.

(81%) and summer (78%) seasons (Figures 10–12, factors 1–4).

This result is in agreement with the analysis of the FM/S scatterplot above (Figure 5C): the FM/S ratio is about the same for the winter and summer seasons because of the opposite annual cycle of the major S sources. The summer S factor has much lower concentrations of black carbon than the winter factors (Figure 8, factors 2 and 4). Therefore, black carbon contribution to the total mass is related mostly to the first and second combustion sources. It is higher in winter than in the summer, and thus, the slope for the linear regression fit for FM/BC is lower for the winter group of points than for the summer (Figure 5B). The PMF model tends to underestimate the measured fine particle mass in March–April and overestimates it in June–November (Figure 9). This indicates that there could be some other aerosol species (such as NH_4NO_3) in the spring season that are not described well by the PMF model. Overall performance of the PMF model is good, with a squared correlation coefficient for the reconstructed mass fit equal to 0.97.

The contribution from the Zn–Pb factor (incineration and smelting) to the total mass was equal to 7.0 ± 1.7% (Figure 10, factor 5). The winter and summer values were equal to 8.7 ± 2.0% and 5.0 ± 1.7%, respectively (Figures 11 and 12, factor 5). Seasonality in meteorological conditions, such as temperature inversions and local wind direction, could also provide higher concentrations of primary particles related to the winter combustion sources and the Zn–Pb factor during the winter season.

The factor with the highest Pb and Mn loadings that represent motor vehicles and Mn smelting contribute less than 3% to the fine mass (Figure 10, factor 6). Soil represents about 4% of the total fine mass (Figure 10, factor 7). Finally, sources associated with As and Cu smelting, Na–S aerosol, and salt together account for less than 4% of the total fine mass (Figure 10, factors 8–11); 8.9 ± 20.5% of the total fine mass in the summer season was not described by the PMF model (Figure 12).

Trajectory Data and Potential Source Contribution Function. A set of airmass backward trajectories had been previously calculated for the Underhill, VT, site for 1989–1996 covering about 95% of the dates for which fine particle data and PMF results were available. These air parcel trajectories were calculated using the CAPITA Monte Carlo model (*19*) with the NGM (*20*) meteorological database and include backward trajectory (horizontal and vertical location) positions for each of 10 hypothetical particles released every 2 h from the receptor location. The individual CAPITA Monte Carlo trajectories were expressed as a series of latitude–longitude coordinates with an initial location 1 h upwind of the receptor location, followed by additional coordinates every 3 h backward in time for 5 days. Details of these air mass history calculations are described in detail by Poirot et al. (*21*).

The construct of the potential source contribution function can be described as follows: if a trajectory end point lies at a cell of address (i, j), the trajectory is assumed to collect material emitted in the cell. Once aerosol is incorporated into the air parcel, it can be transported along the trajectory to the receptor site. The objective is to develop a probability field suggesting likely source locations of the material that results in high measured values at the receptor site. The PSCF methodology has been described previously (*23*, *24*) and will only be summarized here.

The number of end points falling into a single grid cell is $n_{i,j}$. Some of these trajectory end points are associated with sampling intervals when the greater contribution of a particular source is equal to that of the 60th percentile value in the distribution of that species. The choice of this criterion values was made based on trial and error. In many prior applications, the mean value was used for the criterion value, but in this case, the use of the 60th percentile criterion produced results that appeared to correspond better with known emission source locations. The number of end points is $m_{i,j}$. The potential source contribution function (PSCF) is then defined as

$$\mathrm{PSCF}_{ij} = \frac{m_{ij}}{n_{ij}} \tag{7}$$

Thus, the potential source contribution function can be interpreted as a conditional probability describing the spatial distribution of probable geographical source locations inferred by using trajectories arriving at the sampling site. Cells related to the high values of potential source contribution function are the potential source areas. However, the potential source contribution function maps do not provide an emission inventory of a pollutant but rather show those source areas whose emissions can be transported to the measurement site.

To reduce the effect of small values of n_{ij}, an arbitrary weight function $W(n_{ij})$ is multiplied into the PSCF value to better reflect the uncertainty in the values for these cells:

$$W_{ij} = \begin{cases} 1.00 & 1800 < n_{ij} \\ 0.70 & 200 < n_{ij} \le 1800 \\ 0.42 & 100 < n_{ij} \le 200 \\ 0.17 & n_{ij} \le 100 \end{cases} \tag{8}$$

The set of trajectory data contained 12 trajectories for the 10 random air parcels calculations for each day of the 853 days of sampling. There are 37 end points in each trajectory. Therefore, the total number of the end points was 12 × 10 × 853 × 37 or about 3.8×10^6. The grid covers most of North America with 2966 cells of 1° × 1° latitude and longitude so that in average there are $3.8 \times 10^6/2966$ or about 1280 end points per cell. However, the number of the end points per cell for most of the cells of the domain covering likely source areas is much higher. This number also depends on the prevailing wind pattern in the area of sampling. Therefore,

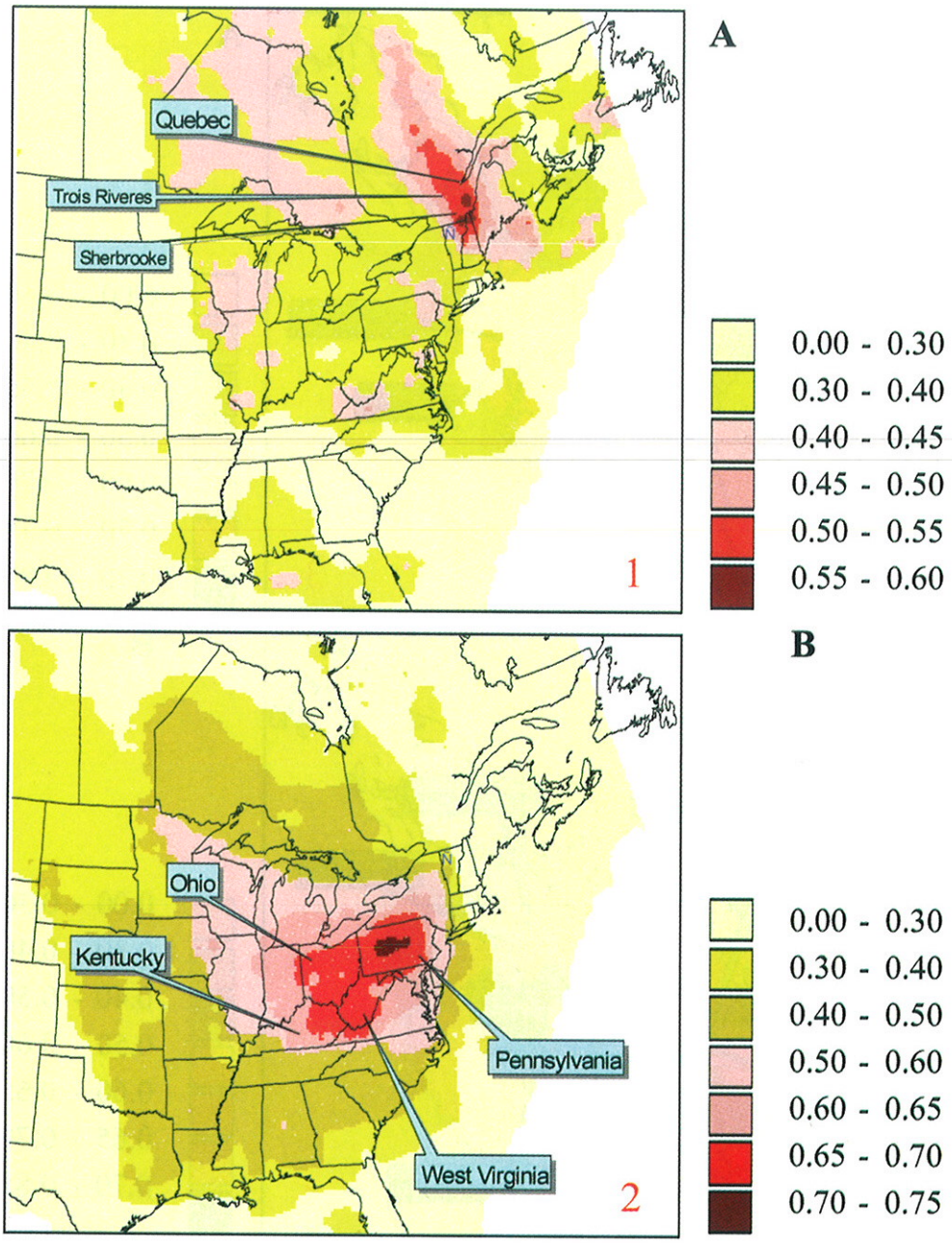

FIGURE 13. Potential source contribution function plots for the wood (A) and the midwestern coal (B) combustion factors. Red numbers represent the corresponding PMF factor numbers. Blue symbols show the location of the sampling site in Underhill, VT.

the 1800, 200, and 100 cutpoint values for the weighting function represent relatively small numbers, and it was found that the number of end points per cell less than 1600−2000 could produce PSCF values with high uncertainty and result to unrealistic attribution of source areas. These weighting function values were obtained empirically by running the PSCF program many times.

PSCF identifies locations more likely to be upwind if receptor concentrations are high (top 40% of days) than they are on an every day basis. These upwind regions of highest probability are typically interpreted as locations with emissions contributing to impacts at the receptor. However, for secondary pollutants formed in the atmosphere, identified upwind regions may also include areas where secondary formation is enhanced in addition to areas where the primary emissions originate. High potential source contribution function regions should coincide with known emissions regions within the domain. However, a region with a low value of the potential source contribution function does not necessarily indicate low emissions from the region since they may not be transported to the receptor site.

The PSCF plots are shown in Figures 13−18. The time series for the wood combustion factor indicates a general winter maxima consistent with residential wood burning but also shows occasional summer spikes, several of which coincide with periods of known forest fires in western Quebec (Figure 7, factor 1). Its PSCF plot shows high probability in the area immediately north of the receptor site, indicating a strong local source influence from residential wood combustion in northern New England and southwestern Quebec (Figure 1A). It could also be related in part to wood combustion and related sources in the Montreal, PQ, metropolitan area.

The PSCF plots for the two coal combustion factors (Figures 13B and 14B) show large common source areas extending from the lower Great Lakes to the south of the

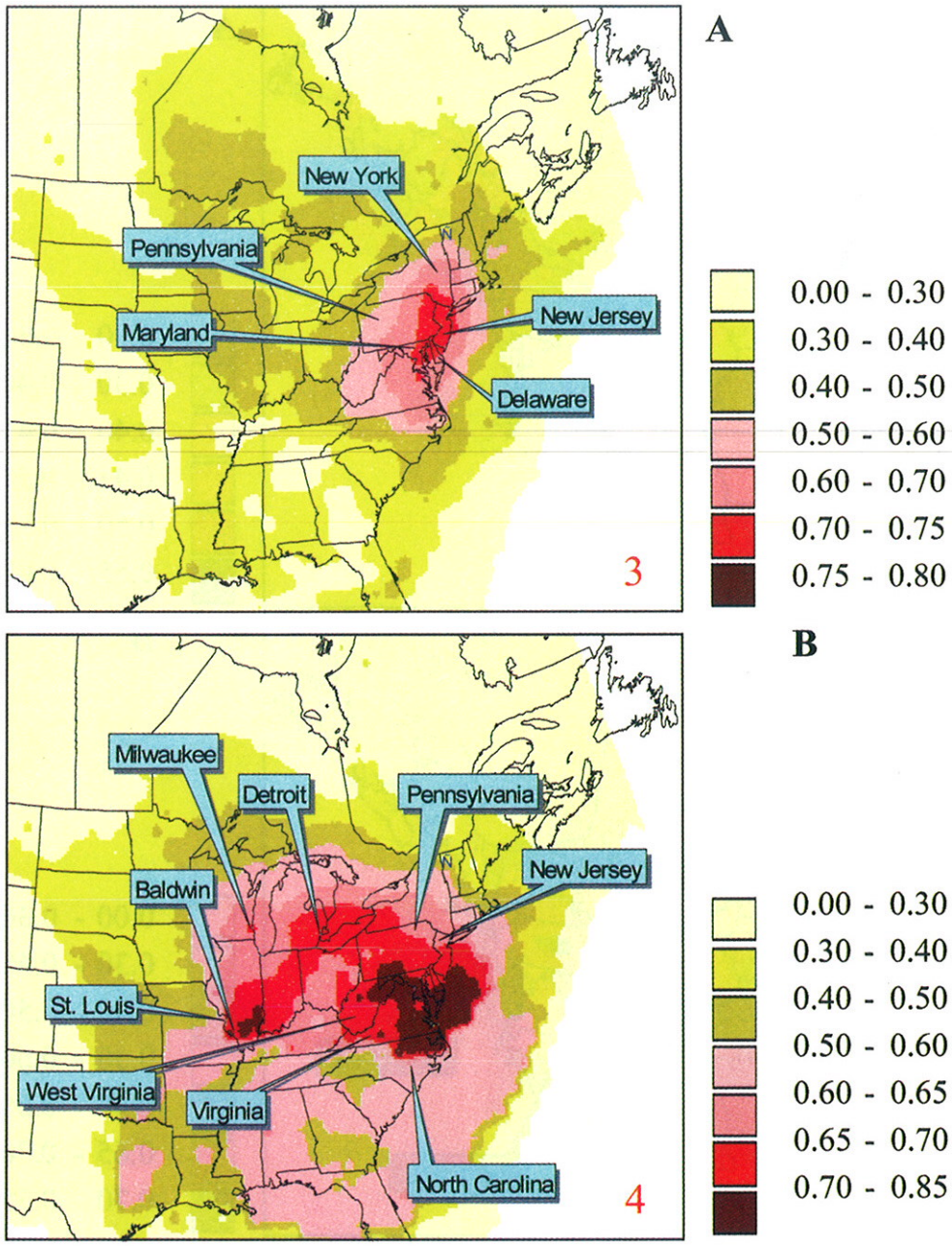

FIGURE 14. Potential source contribution function plots for the east coast oil combustion factor (A) and the midwestern coal combustion plus secondary sulfate formation factor (B). Red numbers represent corresponding PMF factor numbers. Blue symbols show the location of the sampling site in Underhill, VT.

Ohio River Valley, encompassing the locations of many large electricity-generating plants and industrial sources. The first S factor has an annual cycle with maxima during the winter/spring season and source profile with high loadings of S and Se (Figures 7, 8, factor 2). The highest PSCF values (0.70–0.75) for this factor were obtained for central Pennsylvania (Figure 13B). Potential source areas with PSCF higher 0.65 for this factor include Pennsylvania, West Virginia, Ohio, and eastern Kentucky. In addition to these regions, areas of PSCF larger than 0.6 include western New York, Virginia, Indiana, and southern Michigan. It agrees with sulfur dioxide emission area in the U.S. Environmental Protection Agency inventory (*24*).

The time series for the second sulfur factor shows maxima in the summer indicating that this coal combustion factor includes the more efficient secondary sulfate aerosol formation in the summer (Figure 7, factor 4). The area of PSCF higher than 0.6 for the summer coal factor is larger than for the winter coal factor, indicating secondary sulfate formation over the larger areas extending from Illinois to the east coast of the United States (Figure 14B). However, in contrast to the winter factor, the areas of highest PSCF (>0.7) are shifted toward the south east covering eastern Virginia, northern West Virginia, southern Pennsylvania, Maryland, and Delaware (Figure 14B). A high PSCF value area was also found in southern Illinois. It could be related to emissions from facilities at Baldwin and Coffeen (Figure 14B). These sources are known large emitters of SO_2.

The V and Ni factor represents emissions from oil combustion. This factor time series has maxima in the winter–spring season and minima in the summer (Figure 7, factor 3). High PSCF areas lie along the east coast of the United States including eastern Virginia and Pennsylvania as well as southern New York, New Jersey, Maryland, and

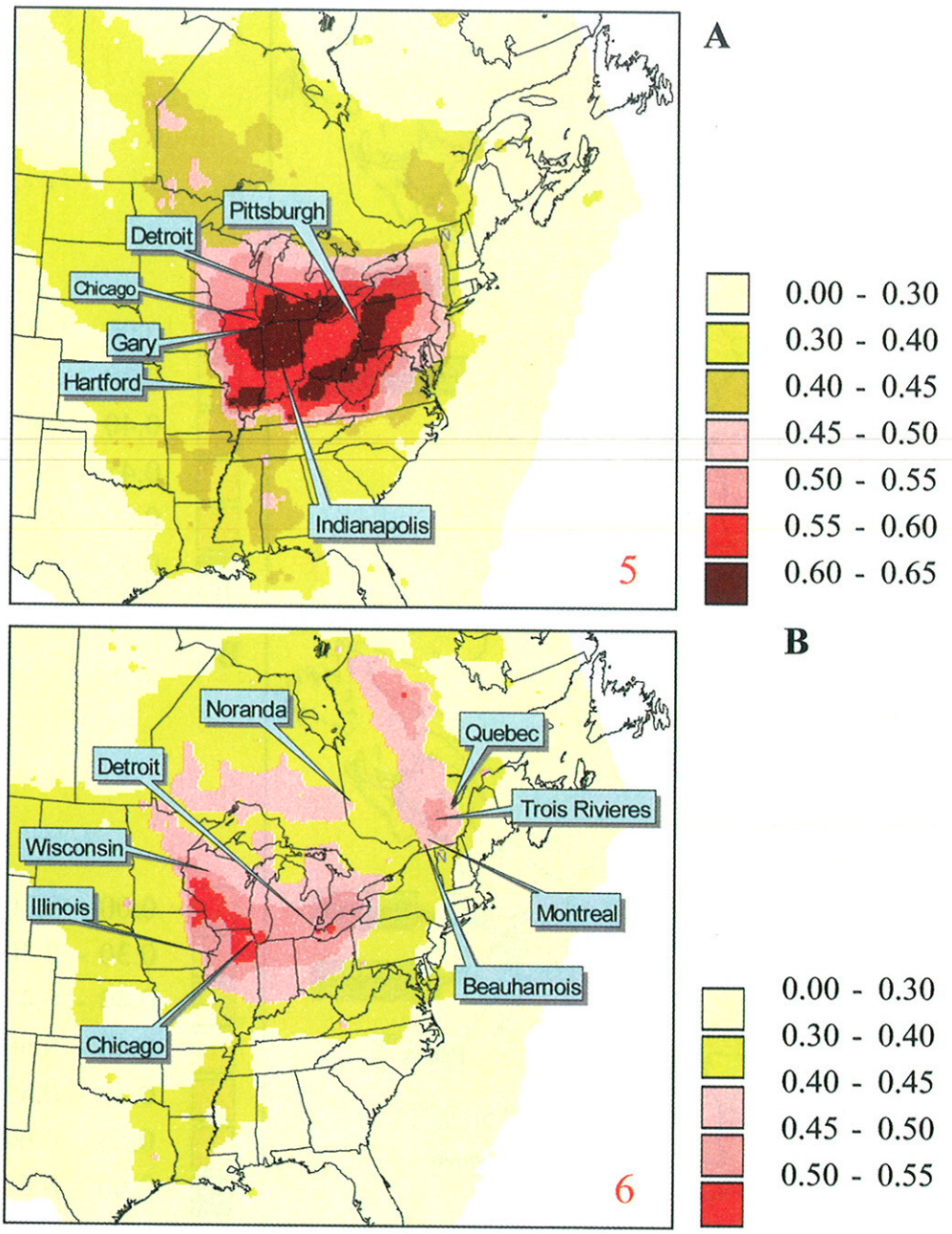

FIGURE 15. Potential source contribution function plots for the Zn−Pb (A) and the Canadian Mn (B) factors. Red numbers represent corresponding PMF factor numbers. Blue symbols show the location of the sampling site in Underhill, VT.

Delaware (Figure 14A). These regions are known locations of oil-fired power plants (*24*).

The fifth factor has high loadings of Zn, Pb, H, BC, and S (Figure 8, factor 5). It was identified as an incineration factor. A PSCF plot is presented in Figure 15A. It can be seen that there is an influence from the local urban sources north of Vermont, in the vicinity of Montreal, PQ, but the PSCF values for these areas do not exceed 0.45 (Figure 15A). At the same time, the PSCF plot shows the large midwestern industrial regions are also potential sources. The highest PSCF areas are found in northern Indiana, southern Michigan, southern Illinois, western Pennsylvania, and areas along the southern border of Ohio (Figure 15A). Some of these areas represent urban incineration sources, for example, the Detroit and Chicago areas. Other areas most likely related to metal production industries. High PSCF values in Illinois could be connected to the secondary nonferrous metals production in Hartford, IL, and steel production in Granite City, IL. This companies are the fourth and the ninth largest, respectively, emitters of lead in the country (*24*). Northern Indiana and southern Ohio are also known locations of metal industry facilities. The high PSCF areas most likely related to major companies in these area, such as steel plants in the vicinity of Steubenville, OH; Gary, IN; and Chesterton, IN. Thus, the Pb−Zn factor appears to represent both municipal waste incineration and metal production industries in the Midwest.

The Canadian motor vehicles and Mn smelting factor has high S, Pb and Mn concentrations (Figure 8, factor 6). The PSCF plot (Figure 15B) shows high probability areas in the Montreal region. Canadian motor vehicles burn gasoline with MMT. In addition, a large Mn alloy production plant southwest of Montreal in Beauharnois, PQ, may have also been an important Mn source. Lorander and Zayed (*25*) compared the atmospheric concentrations of Mn, Pb, and suspended particulates (TSP) in Montreal and showed that both motor vehicles and a ferromanganese plant near

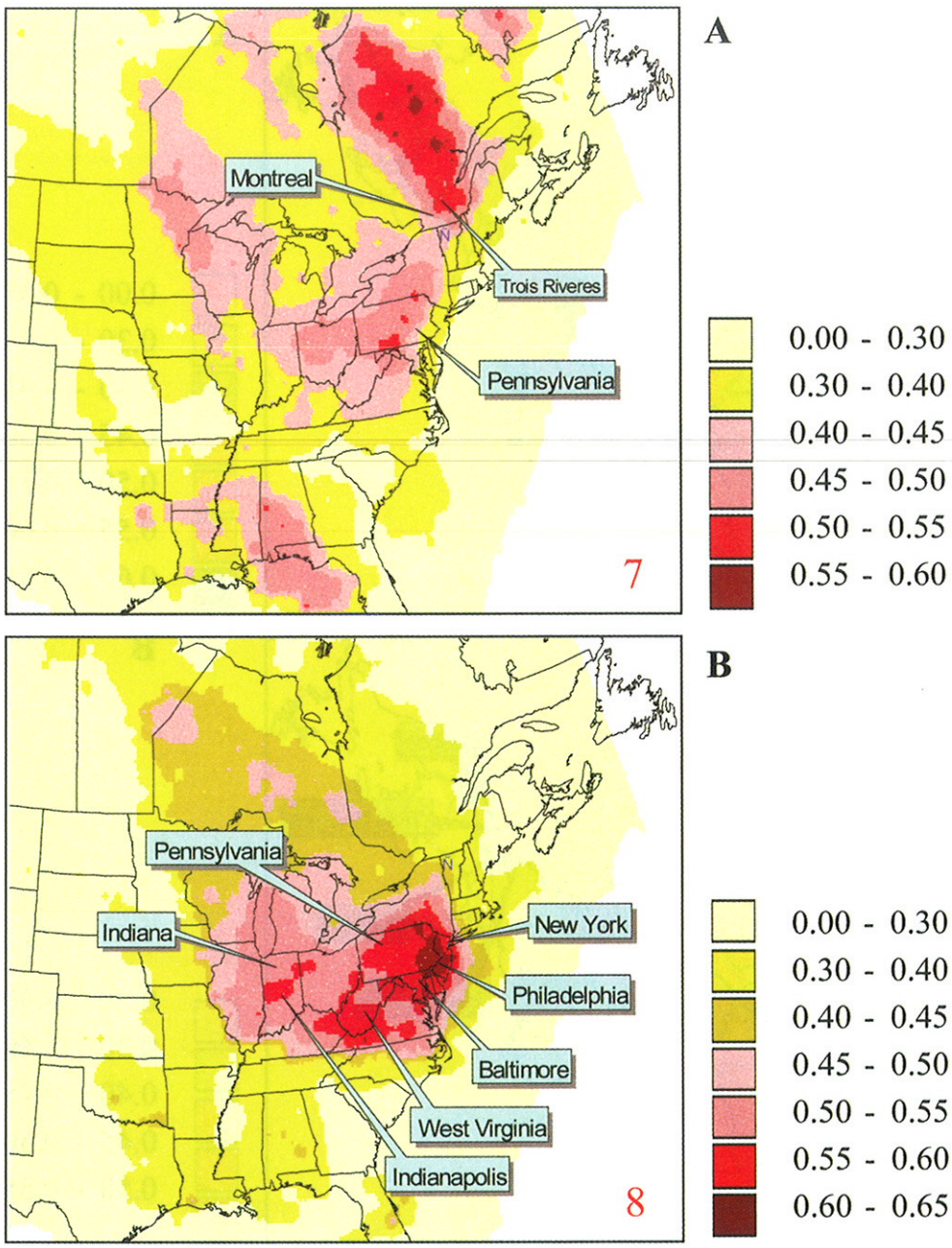

FIGURE 16. Potential source contribution function plots for the soil factor (A) and the smelting of nonferrous metal ores factor (Cu−Zn) (B). Red digits represent corresponding PMF factor numbers. Blue symbols show the location of the sampling site in Underhill, VT.

Montreal are the major sources of Pb and Mn. Their results indicated a decrease in Mn concentrations observed since 1991 attributed to the closing of the ferromanganese plant in Beauharnois, PQ (*25*). A similar change in the Mn concentrations can be observed in Figure 8. Lead and manganese can also be emitted by various industrial processes in the Great Lakes region on both sides of the border. High PSCF areas for the Pb−Mn factor in the Midwest could be related to the steel production industries. Parekh and Husain (*26*) showed that three types of point sources account for most of the noncrustal Mn emissions in the United States. These sources are iron and steel mills, ferro- and sillico-manganese alloy plants, and plants producing Mn metal, synthetic pyrolusite, and Mn chemicals (*26*). Anthropogenic Mn in aerosols at Mayville, a rural site in New York State, were found to originate mostly from the numerous iron and steel industries of the Midwest (*26*). These results agree with the PSCF results for Underhill, VT, shown in Figure 15B. The highest PSCF values are obtained for the southwest of Wisconsin and the northeast of Illinois (Figure 15B). These potential source areas could be related to emissions from the metal production facilities in northern Illinois and Indiana (Sterling, IL; Riverdale, IL; North Chicago, IL; and East Chicago, IN).

The PSCF plot for the soil factor shows high PSCF areas in Canada north of Vermont (Figure 16A). These results again suggest relatively local sources of soil aerosol. Since exposed soil is suspended in the air as a function of wind speed but much of the airborne soil is suspended road dust, it is likely that those trajectories associated with high wind speeds and extending to the edges of the study area provide larger influence on high PSCF for the soil factor than for other factors. Dust emissions from relatively distant regions to the southwest and west appear to be significant contributors, but there are also fine soil contributions associated with dry conditions and high wind speeds from a wide range of

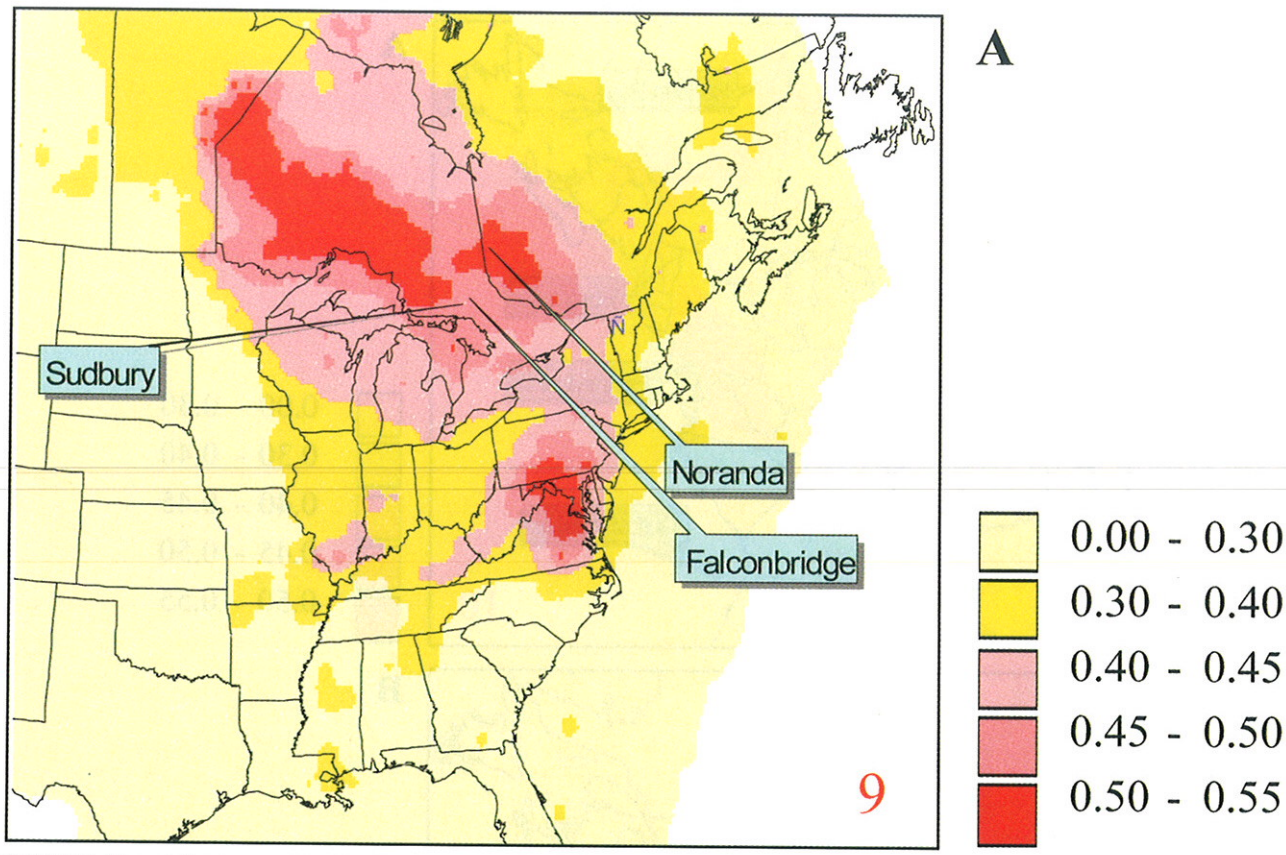

FIGURE 17. Potential source contribution function plot for the As factor representing smelting in Canada. Red numbers represent corresponding PMF factor numbers. Blue symbols show the location of the sampling site in Underhill, VT.

TABLE 2. Sources of Aerosol in Vermont, Their Relative Mass Contributions, and Geographical Locations

PMF factors	high loadings	mass contribution (%) total	mass contribution (%) winter	mass contribution (%) summer	main sources	potential source locations
1	BC, H, K	14.5 ± 5.0	18.4 ± 5.9	9.9 ± 3.8	wood burning, other combustion sources	northern New England and southwestern Quebec
2	BC, H, S, Se	7.1 ± 4.3	9.7 ± 4.9	4.1 ± 3.5	coal combustion, other combustion sources	PA, WV, OH, and eastern KY
3	H, Ni, S, V	6.6 ± 2.6	8.4 ± 3.0	4.4 ± 2.1	oil combustion	eastern VA and PA, southern NY, NJ, MD, and DE
4	H, S	51.3 ± 19.4	44.3 ± 18.9	59.6 ± 19.6	coal combustion plus photochemically enhanced sulfate production from SO_2, other combustion sources	area from IL to the east coast of the United States
5	BC, H, Pb, Zn	7.0 ± 1.7	8.7 ± 2.0	5.0 ± 1.2	municipal waste incineration and nonferrous metal smelting	Midwest
6	BC, K, Mn, Pb	2.1 ± 1.9	2.7 ± 2.4	1.4 ± 1.3	Canadian motor vehicles and Mn smelting, metal production	Midwest, Quebec, Ontario
7	Al, Fe, H, Si, Ti	3.9 ± 1.6	3.5 ± 1.6	4.3 ± 1.6	soil particles, coal combustion	Quebec, Midwest
8	Cu, H, S, Zn	1.5 ± 0.8	1.7 ± 1.0	1.2 ± 0.7	smelting of nonferrous metal ores	east coast of the U.S., IN and WV
9	As, BC, H, S	1.2 ± 1.0	1.4 ± 1.2	0.8 ± 0.8	smelting and coal combustion	Ontario, western Quebec, MD
10	BC, Ca, Fe, Mg, Na, S, V	0.6 ± 0.8	0.9 ± 1.1	0.3 ± 0.5	sea salt, road salting, emissions from industrial sources	Pacific and Arctic Oceans, Gulf of Mexico, southern NY, PA, VA, WV, and IN
11	BC, Cl, Mg, Na, S	0.2 ± 0.6	0.3 ± 0.8	0.1 ± 0.3	industrial sources, road salting	Midwest, KY, IN

locations. Coal combustion emissions with high Si and Al loadings as well as soil emissions could provide some contribution to the observed high PSCF values in the Midwest (Figure 16A).

The major areas of high potential source contribution function for the Cu smelting factor lie along and off the east coast of the United States (Figure 16B). There are also high PSCF value areas in Indiana and West Virginia. This factor could represent nonferrous metal smelting in these areas. High PSCF values in Indiana could represent emissions from the Indianapolis area. High copper loadings related to the municipal waste incineration were seen in aerosol in New York City (*27*). Thus, incineration and various types of metal working in New York City, Philadelphia, Baltimore, Washington, DC, and other cities could be related to the high values of the potential source contribution function for the Cu smelting factor.

The PSCF map for the As factor (factor 9) show potential sources in the eastern regions of Ontario and western Quebec (Figure 17). The third high potential area is found in Maryland. The area in Quebec may come from a single large smelter located near the town of Noranda near the Quebec/Ontario border. It was shown that Canadian smelters and midwestern coal combustion sources are the major sources of As in

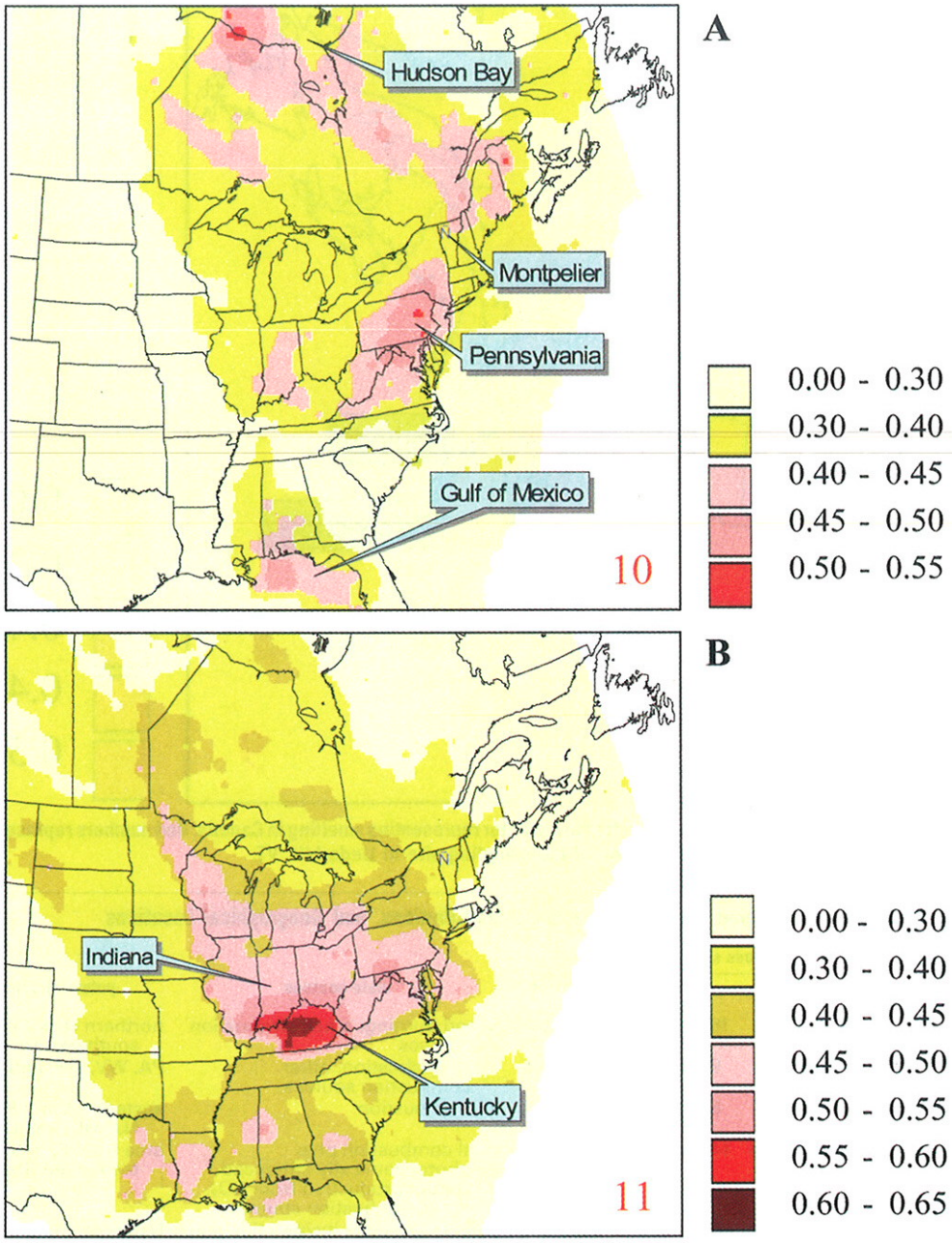

FIGURE 18. Potential source contribution function plots for the Na−S factor (A) and the salt factor (B). Red numbers represent the corresponding PMF factor numbers. Blue symbols show the location of the sampling site in Underhill, VT.

Underhill, VT (*28*). The result shown in Figure 17 agrees with these observations reported before. Nonferrous metal smelters account for the major atmospheric emission of As in Canada. Two large As sources are located in Sudbury and Falconbridge, ON (*29*). There is a trail of moderate areas out the Ohio River Valley from coal-fired power plants. The potential sources for the As factor in Maryland (Figure 17) are unknown. They could be related to the coal combustion emissions and/or emissions from the incineration in the region. Coal-fired power plants in Chalk Point, MD, and Alexandria, VA, could be associated with the high PSCF area in Maryland.

The three major areas showed high PSCF values for the Na−S factor (Figure 18A). The time series for the Na−S factor have maxima in the winter season and minima in the summer (Figure 7, factor 10). Long-range transport from the Pacific and Arctic Oceans could contribute to the Na in this factor. Reaction with H_2SO_4 during the aerosol transport could be the cause for the Cl deficit and excess of S in the Na−S factor. The second potential source area for the Na−S factor is southern New York, Pennsylvania, Virginia, West Virginia, and Indiana (Figure 18A). Emissions from the oil combustion and incineration could be related to aerosol with high loadings of Na and S (*10*). Finally, the third potential source area for the Na−S factor is the Gulf of Mexico (Figure 18A). This region could provide the long-range transported sea salt aerosol observed in Vermont.

The PSCF plot for the salt factor is shown in Figure 18B. Although this factor included sea salt elements such as Mg and K, the highest PSCF values are observed in Kentucky. Thus, the PSCF results would suggest that the Na−S factor was more related to sea salt while this salt factor could be due to transport of particles with high loadings of S, Na and Cl from midwestern industrial sources. The potential sources in Kentucky are unknown. However, there are also areas of moderate potential in the Gulf of Mexico and over the

midwestern United States suggesting the transport of Pacific maritime air across the country.

Table 2 provides the summary of the results presented above. It describes the 11 sources of aerosol in Vermont and presents their relative mass contributions and geographical locations.

Thus, 11 sources of aerosol were identified by the PMF model. Emissions from different anthropogenic activities as well as the secondary aerosol production are the main sources of aerosol measured in Vermont. The black carbon factor represents emissions from wood burning. Two factors with the high sulfur loadings represent sulfate aerosol emissions from coal-fired power plants and the emissions plus photochemically enhanced sulfate production from SO_2. A factor with the highest S–V–Ni loadings represents emissions from the oil-fired power plants. A trend in the oil factor concentrations equal to $-5.5 \pm 0.5\%\ yr^{-1}$ was obtained indicating a reduction of emissions from oil-fired power plants over the sampling period. The first three combustion factors peaked in the winter while the second S factor peaked in the summer. A factor with high concentrations of Zn–Pb represent particles from incineration and other smelting or metal working sources. Other sources of aerosol, emissions from motor vehicles, Cu smelting, As smelting, emissions of aerosol with high S and Na loadings as well as soil and salt particles were also identified. Fuel combustion, local wood smoke, municipal waste incineration, and secondary sulfate production collectively accounted for about 87% of the fine mass concentrations measured in Vermont.

The source areas for 11 identified major sources of aerosol in Vermont were suggested by the potential source contribution function method. The PSCF plot for the wood combustion factor shows high probabilities in the area north of the sampling site, indicating a strong local source influence from residential wood combustion in northern New England and southwestern Quebec. Similar large potential source areas in the midwestern United States were identified for the two coal combustion factors. A larger high potential function domain was obtain for the summer factor showing secondary aerosol formation over the larger area. The midwestern United States was identified as major source for the Zn–Pb factor. Oil combustion emissions are from the power plants along the east coast of the United States. The map for the Pb–Mn factor suggests high probabilities over the nearby Montreal urban area and the areas in the midwestern United States. The windblown dust emissions from local areas to the north are significant contributors for the soil factor. Canadian smelters are the main source areas for the As factor. Long-range transport from the north of Canada and from the Gulf of Mexico are the main sources for the sea salt particles. It is concluded that the combination of the two receptor modeling methods—PMF and PSCF—provides an effective approach to the identification of atmospheric aerosol sources and their locations.

Acknowledgments

The work at Clarkson University was supported by the National Science Foundation under Grant ATM 9523731. We thank Paul Wishinski and Bret A. Schichtel for providing the backward trajectories for the PSCF analysis and Joe Pinto for his helpful comments and suggestions.

Literature Cited

(1) Charlson, R. J.; Schwarz, S. E.; Hales, J. M.; Cess, R. D.; Coakley, J. A., Jr.; Hansen, J. E.; Hofman, D. J. *Science* **1992**, *255*, 423–430.
(2) Hopke, P. K. *Chemom. Intell. Lab. Syst.* **1991**, *10*, 21–43.
(3) Paatero, P.; Tapper U. *Environmetrics* **1994**, *5*, 111–126.
(4) Poirot, R. L.; Wishinski, P.; Hopke, P. K.; Polissar, A. V. *Environ. Sci. Technol.* **2001**, *35*, 4622–4636.
(5) Malm, W. C.; Sisler, J. F.; Huffman, D.; Eldred, R. A.; Cahill, T. A. *J. Geophys. Res.* **1994**, *99*, 1347–1370.
(6) Cahill, T. A.; Eldred, R. A.; Feeney, P. J. *Particulate Monitoring and Data Analysis for the National Park Service 1982–1985*; NPS Contract USDICX-3-0056; U.S. Goverment Printing Office: Washington, DC, 1986.
(7) Flocchini, R. G.; Cahill, T. A.; Eldred, R. A.; Feeney, P. J. *Transactions: A&WMA/EPA Specialty Conference on Visibility and Fine Particles*; Mathai, C. V., Ed.; Estes Park, CO, 1990.
(8) Horvath, H. *Atmos. Environ.* **1993**, *27A*, 293–317.
(9) Watson, J. G.; Chow, J. C.; Lowenthal, L. C.; Pritchet, C. A.; Frazier, C. A.; Neuroth, G. R.; Robbins, R. *Atmos. Environ.* **1994**, *28*, 2493–2505.
(10) Olmez, I.; Sheffield, A. E.; Gordon, G. E.; Houck, J. E.; Pritchett, L. C.; Cooper, J. A.; Dzubay, T. G.; Bennett, R. L. *JAPCA* **1988**, *38*, 1392–1402.
(11) Mason, B. *Principles of Geochemistry*, 3rd ed.; John Wiley & Sons: New York, 1966.
(12) Cooper, J. A.; Redline, D. C.; Sherman, J. R.; Valdovinos, L. M.; Pollard, W. L.; Scavone, L. C.; Badgett-West, C. *PM10 Source Composition Library for the South Coast Air Basin, Volume I: Source Profile Development Documentation Final Report*; NEA report, prepared for South Coast Air Quality Management District: El Monte, CA, July 15, 1987.
(13) Paatero, P. *Chemom. Intell. Lab. Syst.* **1997**, *37*, 15–35.
(14) Polissar, A. V.; Hopke, P. K.; Paatero, P.; Malm, W. C.; Sisler, J. F. *J. Geophys. Res.* **1998**, *103* (D15), 19045–19057.
(15) Anttila, P.; Paatero, P.; Tapper, U.; Järvinen, O. *Atmos. Environ.* **1995**, *29*, 1705–1718.
(16) Hopke, P. K.; Lamb, R. E.; Natusch, D. F. C. *Environ. Sci. Technol.* **1980**, *14*, 164–172.
(17) Loranger, S.; Zayed, J. *Atmos. Environ.* **1994**, *28*, 1645–1651.
(18) Parekh, P.; Hussain, L. *Atmos. Environ.* **1990**, *24A*, 415–421.
(19) Schichtel, B. A.; Husar, R. B. *J. Air Waste Manage. Assoc.* **1996**, *47*, 331–343.
(20) Rolph, G D. *NGM Archive TD-6140*, January 1991–June 1996; Prepared for National Climatic Data Center (NCDC): 1996.
(21) Poirot, R.; P. Wishinski, B.; Schichtel, P. *Girton Air Trajectory Pollution Climatology for the Lake Champlain Basin*; Manley, T., Manley, P., Eds.; AGU Water Monograph on Lake Champlain Research and Implementation; American Geophysical Union: Washington, DC, 1999.
(22) Cheng, M.-D.; Hopke, P. K.; Barrie, L.; Rippe, A.; Olson, M.; Landsberger, S. *Environ. Sci. Technol.* **1993**, *27*, 2063–2071.
(23) Zeng, Y.; Hopke, P. K. *Atmos. Environ.* **1989**, *23*, 1499–1509.
(24) U.S. Environmental Protection Agency, Office of Air Quality Planning & Standards Information Transfer & Program Integration Division, Information Transfer Group Research, Triangle Park, NC 27711, http://www.epa.gov.airsdata.
(25) Loranger, S.; Zayed, J. *Atmos. Environ.* **1994**, *28*, 1645–1651.
(26) Parekh, P.; Hussain, L. *Atmos. Environ.* **1990**, *24A*, 415–421.
(27) Kneip, T. J.; Mallon, R. P.; Kleinman, L. P. *Atmos. Environ.* **1983**, *17*, 299–304.
(28) Rahn, K. A.; Lowenthal, D. H. *Science* **1985**, *228*, 275–284.
(29) Wyche, C. *Mineral Industries of Canada, Australia, and Oceania*; Mineral Perspectives Series; Bureau of Mines, U.S. Department of Interior: Washington, DC, 1989.

Received for review January 29, 2001. Revised manuscript received July 5, 2001. Accepted July 12, 2001.

ES0105865